

Quarterly Technical Report

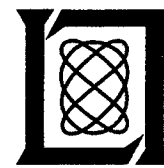
Solid State Research

1997:3

Lincoln Laboratory

MASSACHUSETTS INSTITUTE OF TECHNOLOGY

LEXINGTON, MASSACHUSETTS



Prepared for the Department of the Air Force under Contract F19628-95-C-0002.

Approved for public release; distribution is unlimited.

19980209 096

DTIC QUALITY INSPECTED 4

This report is based on studies performed at Lincoln Laboratory, a center for research operated by Massachusetts Institute of Technology. The work was sponsored by the Department of the Air Force under Contract F19628-95-C-0002.

This report may be reproduced to satisfy needs of U.S. Government agencies.

The ESC Public Affairs Office has reviewed this report, and it is releasable to the National Technical Information Service, where it will be available to the general public, including foreign nationals.

This technical report has been reviewed and is approved for publication.

FOR THE COMMANDER

Gary Tutungian
Gary Tutungian
Administrative Contracting Officer
Contracted Support Management

Non-Lincoln Recipients

PLEASE DO NOT RETURN

Permission is given to destroy this document
when it is no longer needed.

**MASSACHUSETTS INSTITUTE OF TECHNOLOGY
LINCOLN LABORATORY**

SOLID STATE RESEARCH

QUARTERLY TECHNICAL REPORT

1 MAY-31 JULY 1997

ISSUED 21 JANUARY 1998

Approved for public release; distribution is unlimited.

LEXINGTON

MASSACHUSETTS

ABSTRACT

This report covers in detail the research work of the Solid State Division at Lincoln Laboratory for the period 1 May through 31 July 1997. The topics covered are Quantum Electronics, Electro-optical Materials and Devices, Submicrometer Technology, High Speed Electronics, Microelectronics, Analog Device Technology, and Advanced Silicon Technology. Funding is provided primarily by the Air Force, with additional support provided by the Army, DARPA, Navy, BMDO, NASA, and NIST.

TABLE OF CONTENTS

Abstract	iii
List of Illustrations	vii
List of Tables	xi
Introduction	xiii
Reports on Solid State Research	xv
Organization	xxvii
1. QUANTUM ELECTRONICS	1
1.1 Optically Pumped Mid-Infrared Semiconductor Laser Technology for Infrared Countermeasures	1
2. ELECTRO-OPTICAL MATERIALS AND DEVICES	3
2.1 Micron-Size Large-Numerical-Aperture Microlenses in GaP Fabricated by Mass-Transport Smoothing of Etched Single Mesa	3
2.2 High-Power 1.5- μ m InGaAsP/InP Lasers with a Tapered Gain Region	8
3. SUBMICROMETER TECHNOLOGY	11
3.1 Optical Lithography with 157-nm Lasers	11
3.2 New Surface Emission Cathode in Diamond	16
4. HIGH SPEED ELECTRONICS	25
4.1 Phase Noise of a Resonant-Tunneling Relaxation Oscillator	25
5. MICROELECTRONICS	31
5.1 Geiger-Mode Avalanche Photodiode Arrays for Imaging Laser Radar	31
6. ANALOG DEVICE TECHNOLOGY	35
6.1 Tunable Superconducting Resonators Using Ferrite Substrates	35

7.	ADVANCED SILICON TECHNOLOGY	39
7.1	Fully Depleted Silicon-on-Insulator Technology Development	39

LIST OF ILLUSTRATIONS

Figure No.		Page
1-1	Power output of broad-area InAsSb double-heterostructure laser.	1
1-2	Power output from the Stirling cooler package shown in Figure 1-1. Solid and dashed lines are experiment and model, respectively. Oscillation and overshoot in the data are due to the power meter response. The pulse length is 100 μ s and the pulse repetition frequency is 2 kHz.	2
2-1	Mass-transport smoothing of periodic array of etched mesas. After a relatively short mass-transport time ($t = 0.1 \tau$) the profile is more spherical near the center and can better approximate a desired lens profile. After a longer time ($t = 0.5 \tau$), the profile becomes purely sinusoidal.	3
2-2	Approximation of micron-size spherical profile by mass-transport smoothing of etched mesa. By choosing suitable mesa width and height, $\Lambda/2$ and $2A$, respectively, for a given mass-transport temperature and time, the spherical profile is well approximated over a useful large aperture.	6
2-3	Scanning electron micrograph of cleaved cross section of fabricated GaP cylindrical microlens: (a) is lower magnification showing the nearly sinusoidal profile formed by a smoothing of etched rectangular mesas, and (b) shows a higher magnification near the center where a nearly constant curvature has been measured.	7
2-4	Device design for 1.5- μ m tapered lasers.	8
2-5	CW output power vs current for 1.5- μ m tapered laser with 1-mm-long ridge input section and 2-mm-long tapered section.	10
2-6	Beam profile in plane of the junction of tapered laser oscillator with 0.9-W cw output.	10
3-1	Comparison of depth of focus at best dose and exposure latitude at best focus, as calculated from aerial image simulations. The printed features are equal lines and spaces, at the dimensions indicated (100, 130, and 150 nm). The imaging configurations are 193 nm at 0.7 numerical aperture (NA), and 157 nm at 0.6 and 0.7 NA, all three with circular illumination and spatial coherence 0.6.	11

LIST OF ILLUSTRATIONS (Continued)

Figure No.		Page
3-2	Measured transmission of fused silica, crystalline calcium fluoride, and crystalline magnesium fluoride, at the respective indicated thicknesses. The broken vertical line indicates the 157-nm wavelength.	12
3-3	Absorption coefficient of calcium fluoride in the range 130–200 nm, as calculated from transmission measurements performed with a vacuum uv spectrophotometer on three prism-shaped samples along their 10- and 40-mm axes, as described in the text. At 157 nm the absorption coefficient is $\sim 0.004 \text{ cm}^{-1}$. The broken vertical line indicates the 157-nm wavelength.	12
3-4	Silicon uptake in the vapor phase silylation of polyvinylphenol as a function of exposure dose at 157 nm (in nitrogen) and 193 nm (in nitrogen and in air). The silylation efficiency is determined by the area under the Si-O-CH _x absorption band measured with a Fourier transform infrared spectrophotometer. Exposure in nitrogen has almost the same effect at the two wavelengths, and is markedly less efficient than 193-nm exposure in air in suppressing silylation.	15
3-5	Scanning electron micrograph of 80-nm lines printed in projection at 157 nm with 0.5-NA objective. The resist process was top-surface imaging in polyvinylphenol, followed by vapor phase silylation and oxygen reactive ion etching. The mask was a 36 \times chromeless edge shifter, fabricated in calcium fluoride.	16
3-6	Triple junction (metal–NEA semiconductor–vacuum) electric field enhancement cathode: (a) shows a cross section of a triple junction formed by the metal–NEA semiconductor–vacuum interface. The lighter region in the semiconductor near the metal-semiconductor interface is the space charge region containing the ionized dopants. (b) is a plot of potential energy along the NEA semiconductor–vacuum interface. Electrons tunnel from the metal substrate onto the NEA semiconductor–vacuum interface.	17
3-7	(a) Schematic diagram of Li ⁺ -implanted diamond with phosphor screen placed on top of the diamond. (b) Observed fluorescence of the phosphor screen. The fluorescence is directly under the portion of the diamond implanted with Li ⁺ . The screen continued to fluoresce when lifted several hundred micrometers above the diamond, but the fluorescing regions moved away from the edge of the diamond to its center and became more diffuse.	18

LIST OF ILLUSTRATIONS (Continued)

Figure No.		Page
3-8	Schematic drawing of surface emission cathode experiment using the cleaved surface of diamond to emit electrons.	19
3-9	Plot of emitted and electrode currents as a function of applied voltage for the structure shown in Figure 3-8.	20
3-10	Energy analysis of emitted electrons. A retarding energy analyzer can be used to estimate the electron's energy, because the electrons are emitted as a collimated beam from the edge of the diamond. The inset shows a schematic drawing of the experiment.	21
3-11	Emission current with and without incandescent illumination from a fiber lamp. The filled circles indicate the normal emission characteristics measured in the dark. The open circles show the effects of illumination on emission. The lower curve was obtained in the dark after 1 min of illumination, and it shows the recovery of the emission after the illumination has been removed. The inset shows a possible explanation of the observed reduction in emission with light, where the illumination neutralizes positive charges near the triple junction.	22
4-1	(a) Circuit diagram and voltage waveforms measured with a sampling oscilloscope having temporal resolution ~ 25 ps. (b) Square wave output representing the voltage across the resonant-tunneling diode (RTD). (c) Pulsed output voltage measured across the load. The load voltage is proportional to the current passing through the RTD.	25
4-2	Injection-locking gain for fundamental and subharmonic locking.	27
5-1	Distribution of photon return times from fixed-range target as measured by an avalanche photodiode.	32
5-2	Mask layout for the MOSIS CMOS timing chip.	32
6-1	Plot of f_0 (open circles, left scale) and Q (closed circles, right scale) vs applied field for a YBCO microstrip resonator on a LaAlO_3 substrate coupled to polycrystalline iron garnet.	36
6-2	Plot of f_0 (open circles, left scale) and Q (closed circles, right scale) vs applied field for a niobium microstrip resonator on a polycrystalline iron garnet substrate.	37

LIST OF ILLUSTRATIONS (Continued)

Figure No.		Page
6-3	Plot of f_0 vs applied field for a niobium microstrip resonator on a polycrystalline iron garnet substrate. Points are measured data and the solid line is the model discussed in the text, with $N_z = 0.02$. The dashed line is for $N_z = 0$.	38
7-1	I_d plots of an <i>n</i> -channel fully depleted silicon-on-insulator (FDSOI) device with (a) 0.25-nm sidewall oxide and (b) 8-nm sidewall oxide. Shown are the initial and postradiation characteristics at 10, 20, 30, 40, 50, and 80 krads. Gate length and width are 0.25 and 7 μm , respectively; drain voltage is 0.05 V.	43
7-2	Ring oscillator stage delay vs extrinsic resistance extracted from test transistors adjacent to the ring oscillator. The sum of the <i>p</i> - and <i>n</i> -channel resistance (diamonds) and the <i>p</i> -channel resistance (squares) indicates that <i>p</i> -channel resistance variations accounted for the majority of delay.	45
7-3	Response surface of a 0.25- μm ring oscillator stage delay vs transistor extrinsic resistance. HSPICE was used to simulate delay using SPICE parameters extracted from FDSOI transistors with the exception of the <i>n</i> - and <i>p</i> -channel resistances which were varied in the simulation.	45

LIST OF TABLES

Table No.		Page
3-1	Optical and Physical Material Parameters at 157 and 193 nm	14
4-1	Phase Noise and Timing Jitter for Fundamental ($N = 1$) Injection Locking at 1.142 GHz	28
4-2	Phase Noise and Timing Jitter for Fundamental ($N = 1/5$) Injection Locking at 228 MHz	28
7-1	Fully Depleted Silicon-on-Insulator Process and Design Parameters	40
7-2	Fully Depleted Silicon-on-Insulator Photolithography Levels	42
7-3	Effects of 10% Process Variations on 0.25- μm Parameters	44
7-4	Effects of 10% Process Variations on 0.15- μm Parameters	46

INTRODUCTION

1. QUANTUM ELECTRONICS

Efforts in the development of mid-infrared semiconductor materials over the last several years have produced laser devices with output power at the ~1-W level in 0.5-ms pulses at the temperature attainable with a compact Stirling cooler. Semiconductor lasers operating in the mid-infrared (2–5 μm) region are suitable for infrared countermeasures applications.

2. ELECTRO-OPTICAL MATERIALS AND DEVICES

A technique has been developed for accurate fabrication of micron-sized lenses by mass-transport smoothing of etched single mesas. A 12- μm cylindrical lens of 0.73 numerical aperture has been formed in a GaP substrate.

High-power diode lasers consisting of a ridge-waveguide section coupled to a tapered region have been fabricated in 1.5- μm InGaAsP/InP multiple-quantum-well material. CW output powers of 0.9 W were obtained with ~80% of the power in the near-diffraction-limited central lobe of the far field.

3. SUBMICROMETER TECHNOLOGY

Projection lithography using a 157-nm wavelength laser illuminator has been evaluated as a possible manufacturing technology for the 100-nm feature-size regime. Optical system design, laser performance, optical materials, and resists were investigated, and an experimental exposure system was used to pattern 80-nm features.

A new type of diamond field emission cathode has been developed based on the triple junction effect. Experimental results support the importance of the diamond-metal-vacuum triple junction in the operation of these devices.

4. HIGH SPEED ELECTRONICS

Experimental results have been obtained for the phase noise of a relaxation oscillator consisting of a resonant-tunneling diode in series connection with a transmission line, one end of which is shorted. The resonant-tunneling relaxation oscillator (RTRO) emits a sequence of sharp current pulses that are mode locked to the fundamental mode of the cavity formed by the short-circuited transmission line, and timing jitter as low as 200 fs was measured for an RTRO that emitted 30-ps pulses at a repetition rate of 1.1 GHz.

5. MICROELECTRONICS

Monolithic arrays of silicon avalanche photodiodes (APDs) for visible (532 nm) Geiger-mode operation have been fabricated for use in imaging laser radar systems that will have subnanosecond timing resolution and single-photon-per-pixel sensitivity, and a MOSIS CMOS chip is being fabricated that will

provide timing electronics for a 4×4 APD array. From our measurements, external quantum efficiencies are in the range of 40% on uncoated front-illuminated devices and timing jitters are 140 ps.

6. ANALOG DEVICE TECHNOLOGY

Tunable microwave resonators combining planar superconducting microstrip circuits with ferrite substrates have been demonstrated. The devices provide tunability of 3% and Q 's as high as 5000.

7. ADVANCED SILICON TECHNOLOGY

Integrated circuits in fully depleted silicon-on-insulator material have been fabricated with $0.25\text{-}\mu\text{m}$ drawn gate length, and a 1-GHz digital chip has been demonstrated. In addition, simulations have been used to define a process compatible with $0.15\text{-}\mu\text{m}$ technology.

REPORTS ON SOLID STATE RESEARCH

1 MAY THROUGH 31 JULY 1997

PUBLICATIONS

Resonant-Tunneling Transmission-Line Relaxation Oscillator	E. R. Brown C. D. Parker S. Verghese M. W. Geis J. F. Harvey*	<i>Appl. Phys. Lett.</i> 70 , 2787 (1997)
Self-Aligned Pseudomorphic HEMT with a Low-Temperature-Grown GaAs Gate Insulator	C. L. Chen L. J. Mahoney S. D. Calawa K. M. Molvar A. R. Calawa	<i>Electron. Lett.</i> 33 , 640 (1997)
External Cavity Mid-Infrared Semiconductor Lasers	H. Q. Le G. W. Turner J. R. Ochoa M. J. Manfra C. C. Cook Y.-H. Zhang*	<i>Proc. SPIE</i> 3001 , 298 (1997)
Degenerate Layer at GaN/Sapphire Interface: Influence on Hall-Effect Measurements	D. C. Look* R. J. Molnar	<i>Appl. Phys. Lett.</i> 70 , 3377 (1997)
Defect Donor and Acceptor in GaN	D. C. Look* D. C. Reynolds* J. W. Hemsky* J. R. Sizelove* R. L. Jones R. J. Molnar	<i>Phys. Rev. Lett.</i> 79 , 2273 (1997)

*Author not at Lincoln Laboratory.

Three-Dimensional Metallodielectric Photonic Crystals Exhibiting Resonant Infrared Stop Bands	K. A. McIntosh L. J. Mahoney K. M. Molvar O. B. McMahon S. Verghese M. Rothschild E. R. Brown	<i>Appl. Phys. Lett.</i> 70 , 2937 (1997)
Growth of Gallium Nitride by Hydride Vapor-Phase Epitaxy	R. J. Molnar W. Götz* L. T. Romano* N. M. Johnson*	<i>J. Cryst. Growth</i> 178 , 147
Performance of Excimer Lasers as Light Sources for 193-nm Lithography	J. H. C. Sedlacek S. P. Doran M. Fritze R. R. Kunz M. Rothschild R. S. Uttaro D. Corliss*	<i>Proc. SPIE</i> 3051 , 874 (1997)
Strain Determination in Heteroepitaxial GaN	B. J. Skromme* H. Zhao* D. Wang* H. S. Kong* M. T. Leonard* G. E. Bulman* R. J. Molnar	<i>Appl. Phys. Lett.</i> 71 , 829 (1997)
Binary Optics Fabrication	M. B. Stern	In <i>Microoptics: Elements, Systems and Applications</i> , P. Herzig, ed. (Institute of Microtechnology, University of Neuchatel, Switzerland, 1997), p. 53

*Author not at Lincoln Laboratory.

Pressure Induced Deep Gap State of Oxygen in GaN	C. Wetzel* T. Suski* J. W. Ager III* E. R. Weber* E. E. Haller* S. Fischer* B. K. Meyer* R. J. Molnar P. Perlin*	<i>Phys. Rev. Lett.</i> 78 , 3923 (1997)
Microchip Optical Parametric Oscillators	J. J. Zayhowski	<i>IEEE Photon. Technol. Lett.</i> 9 , 925 (1997)

ACCEPTED FOR PUBLICATION

Lithography with 157-nm Lasers	T. M. Bloomstein M. W. Horn M. Rothschild R. R. Kunz S. T. Palmacci R. B. Goodman	<i>J. Vac. Sci. Technol. B</i>
40 Gb/s All-Optical Circulating Shift Register Using an Inverting Ultrafast Nonlinear Interferometer	J. P. Donnelly K. L. Hall S. H. Groves	<i>Opt. Lett.</i>
Single-Mode, High-Peak-Power, Passively <i>Q</i> -Switched Diode-Pumped Nd:YAG Laser	T. Y. Fan J. J. Zayhowski R. S. Afzal* A. W. Yu*	<i>Opt. Lett.</i>

*Author not at Lincoln Laboratory.

A New Surface Electron Emission Mechanism in Diamond Cathode	M. W. Geis N. N. Efremow, Jr. K. E. Krohn J. C. Twichell T. M. Lyszczarz R. Kalish [*] J. A. Greer [*] M. D. Tabat [*]	<i>Nature</i>
Theory and Experimental Results of a New Diamond Surface Emission Cathode	M. W. Geis N. N. Efremow, Jr. K. E. Krohn J. C. Twichell T. M. Lyszczarz R. Kalish [*] J. A. Greer [*] M. D. Tabat [*]	<i>Linc. Lab. J.</i>
Hole Traps in Natural Type IIB Diamond	M. W. Geis J. C. Twichell	<i>IEEE Trans. Electron Devices</i>
Diamond Grit Based Field Emission Cathodes	M. W. Geis J. C. Twichell N. N. Efremow K. E. Krohn M. B. Stern T. M. Lyszczarz	<i>Electron Device Lett.</i>
A New Method for Measuring the Thermal Conductivity of Thin Film	S. Govorkov [*] W. Ruderman [*] M. W. Horn R. B. Goodman M. Rothschild	<i>Solid State Technol.</i>
Are Advanced Photoresists Helping to Extend Optical Lithography?	R. R. Kunz	<i>Semicond. Int.</i>

*Author not at Lincoln Laboratory.

Photolithography at 0.13 μm Using ArF Excimer Laser Lithography in Combination with Resolution Enhancement Techniques	R. R. Kunz M. Y. Chan* S. P. Doran M. Rothschild	<i>J. Vac. Sci. Technol. B</i>
Photolithography at 193 nm	M. Rothschild M. W. Horn C. L. Keast R. R. Kunz S. C. Palmateer S. P. Doran A. R. Forte	<i>Linc. Lab. J.</i>
Nanochannel Fabrication for Chemical Sensors	M. B. Stern M. W. Geis J. E. Curtin	<i>J. Vac. Sci. Technol. B</i>

PRESENTATIONS[†]

Diode-Laser-Pumped Solid-State Lasers	T. Y. Fan	Lincoln Laboratory Technical Seminar Series, University of California at Berkeley, Berkeley, California, 9 May 1997
High-Efficiency Zn ₂ SiO ₄ :Mn Thin Film Phosphor for Flat Panel Field Emission Displays	G. Tompa* T. M. Bloomstein S. M. Palmacci M. Rothschild	Society for Information Display, Boston, Massachusetts, 14 May 1997

*Author not at Lincoln Laboratory.

†Titles of presentations are listed for information only. No copies are available for distribution.

How Practical Is 193-nm Lithography?	M. Rothschild	Technical Seminar, Olin Microelectronics Materials, Providence, Rhode Island, 15 May 1997
High-Performance CCD Imagers for Low-Light-Level Applications	E. D. Savoye	Lincoln Laboratory Technical Seminar Series, University of Minnesota, Minneapolis, Minnesota, 15 May 1997
Lattice-Matched Epitaxial GaInAsSb/ GaSb Thermophotovoltaics	C. A. Wang H. K. Choi G. W. Turner M. J. Manfra	3rd National Renewable Energy Laboratory Conference on Thermophotovoltaic Generation of Electricity, Colorado Springs, Colorado, 18-21 May 1997
Diamond Surface Emission Cathodes	M. W. Geis J. C. Twichell T. M. Lyszczarz K. E. Krohn N. N. Efremow	24th IEEE International Conference on Plasma Science, San Diego, California, 18-22 May 1997

40 Gb/s All-Optical Circulating Shift Register Using an Inverting Ultrafast Nonlinear Interferometer	J. P. Donnelly K. L. Hall S. H. Groves	1997 Conference on Lasers and Electro-Optics, Baltimore, Maryland, 18-23 May 1997
Laser-Fabricated Glass Microlens Array	M. Fritze M. B. Stern P. W. Wyatt	
Candidate Laser Transmitters for the Remote Sensing of Atmospheric Water Vapor from the Surface of Mars	M. A. Krainak * D. M. Cornwell * J. J. Coleman * P. D. Dragic * A. Andrawis T. Y. Fan J. J. Zaykowski	
Low-Threshold, High-Temperature Quasi-cw InAs/GaInSb Type-II Quantum Well Lasers	H. Q. Le C.-H. Lin * S. J. Murray * D. Zhang S.-S. Pei * C. L. Felix * J. R. Meyer	
Covering the Spectrum with Passively <i>Q</i> -Switched Nd:YAG Microchip Laser Systems	J. J. Zaykowski	
Microchip Lasers	J. J. Zaykowski	
Field-Emitter Arrays for Inductive-Output Amplifiers	M. A. Hollis C. T. Harris R. H. Mathews C. A. Graves R. A. Murphy	International Conference on Plasma Science, San Diego, California, 19-22 May 1997

* Author not at Lincoln Laboratory.

Lithography with 157-nm Lasers	T. M. Bloomstein M. W. Horn M. Rothschild R. R. Kunz S. T. Palmacci R. B. Goodman	41st International Conference on Electron, Ion and Photon Beams and Nanofabrication, Dana Point, California, 27-30 May 1997
Photolithography at 0.13 μm Using ArF Excimer Laser Lithography in Combination with Resolution Enhancement Techniques	R. R. Kunz M. Y. Chan * S. P. Doran M. Rothschild	
Nanochannel Fabrication for Chemical Sensors	M. B. Stern M. W. Geis J. E. Curtin	
Microchip Lasers	J. J. Zayhowski	
Mid-Infrared Diode Lasers	H. K. Choi G. W. Turner C. A. Wang	Summer School on Miniature Coherent Light Sources in Dielectric Media, Les Houches, France, 2-6 June 1997
Optically Pumped Mid-Infrared Semiconductor Laser Technology for Infrared Countermeasures	H. Q. Le G. W. Turner H. K. Choi V. Daneu T. Y. Fan D. L. Spears A. Sanchez	1997 Diode Laser Technology Review, Albuquerque, New Mexico, 8-12 June 1997
A Comparative Approach in Evaluating Mid-Infrared Sb-Based Laser Materials	H. Q. Le G. W. Turner J. R. Ochoa	

* Author not at Lincoln Laboratory.

Compact Packaging and Efficient Fiber Coupling of Tapered Laser Using a Single Anamorphic GaP Lens	Z. L. Liau J. N. Walpole L. J. Missaggia F. Durville* R. Rediker*	1997 Diode Laser Technology Review, Albuquerque, New Mexico, 8-12 June 1997
Tunable Superconducting Resonators Using Ferrite Substrates	D. E. Oates G. F. Dionne J. A. Weiss	1996 IEEE MTT-S International Microwave Symposium, Denver, Colorado, 8-13 June 1997
Planar Magnetic Circuits and Other Innovations for Microwave Ferrite Devices		
Fully Planar Backend Processing for Sub-0.25- μm Fully Depleted Silicon-on-Insulator Technology	J. M. Knecht C. L. Keast J. H. Reinold, Jr. E. F. Gleason*	1997 VLSI Multilevel Interconnection Conference, Santa Clara, California, 10-12 June 1997
Diamond Surface Emission Cathodes	M. W. Geis N. N. Efremow K. E. Krohn J. C. Twichell T. M. Lyszczarz	55th Annual Device Research Conference, Fort Collins, Colorado, 23-25 June 1997
Uniformity Limits in Arrays of Analog Sense Circuits	D. A. Feld J. P. Sage	
Modeling the Nonlinear Surface Impedance of High- T_c Thin Films	D. E. Oates	
Operation of a Programmable Filter for a 2-Gigachip-per-Second Spread-Spectrum Modem	J. P. Sage D. A. Feld	6th International Superconductive Electronics Conference, Berlin, Germany, 25-28 June 1997

*Author not at Lincoln Laboratory.

Performance Evaluation of 193-nm
Optical Materials

R. R. Kunz
V. Liberman
M. Rothschild
J. H. C. Sedlacek
A. K. Bates
R. Uttaro
A. Grenville
D. Corliss^{*}
R. N. Shagam^{*}

Filamentary Damage Tracks Induced
in Fused Silica by Low Fluence
193-nm Excimer Laser Irradiation

V. Liberman
M. Rothschild
J. H. C. Sedlacek
A. Grenville
D. Corliss^{*}

3rd International Symposium
on 193 nm Lithography,
Onuma, Nanae, Japan,
29 June–2 July 1997

Marathon Damage Testing of Optical
Materials for 193-nm Lithography

V. Liberman
M. Rothschild
J. H. C. Sedlacek
R. Uttaro
A. K. Bates
A. Grenville
D. Corliss^{*}

Beam Propagation Modeling of
Tapered Amplifiers and Lasers

S. R. Chinn
J. N. Walpole

Progress in Electromagnetics
Research Symposium,
Cambridge, Massachusetts,
7-11 July 1997

Microchip Lasers and Applications

J. J. Zaykowski
A. Sanchez
T. Y. Fan

Solid State Lasers, Laser-
Materials and Applications,
Tianjin, China,
8-11 July 1997

* Author not at Lincoln Laboratory.

High-Power 1.3- and 1.5- μ m InGaAsP/ InP Lasers and Amplifiers with Tapered Gain Regions	J. N. Walpole G. E. Betts J. P. Donnelly S. H. Groves	International Workshop on Fundamentals, Modeling and Control of Semiconductor Lasers, Cork, Ireland, 20-25 July 1997
Future Trends in DUV Lithography	R. R. Kunz	Semicon West, San Francisco, California, 21 July 1997
Large-Format Low-Light-Level CCD Imager with Advanced Signal Processing	B. E. Burke R. K. Reich E. D. Savoye A. M. Waxman	1997 Meeting of Infrared Information Symposium Specialty Group, Monterey, California, 30-31 July 1997

ORGANIZATION

SOLID STATE DIVISION

D. C. Shaver, *Head*
R. W. Ralston, *Associate Head*
N. L. DeMeo, Jr., *Assistant*
Z. L. Lemnios, *Senior Staff*
J. W. Caunt, *Assistant Staff*
K. J. Challberg, *Administrative Staff*
J. D. Pendergast, *Administrative Staff*

SUBMICROMETER TECHNOLOGY

M. Rothschild, *Leader*
T. M. Lysczarz, *Assistant Leader*
L. H. Dubois, *Senior Staff*[†]

Astolfi, D. K.
Bloomstein, T. M.
Craig, D. M.
DiNatale, W. F.
Doran, S. P.
Efremow, N. N., Jr.
Forte, A. R.
Geis, M. W.
Goodman, R. B.
Horn, M. W.
Krohn, K. E.

Kunz, R. R.
Liberman, V.
Maki, P. A.
Palmacci, S. T.
Palmateer, S. C.
Reinold, J. H., Jr.
Sedlacek, J. H. C.
Stern, M. B.
Twichell, J. C.
Uttaro, R. S.

QUANTUM ELECTRONICS

A. Sanchez-Rubio, *Leader*
T. Y. Fan, *Assistant Leader*

Dill, C., III
Jeys, T. H.
Le, H. Q.
Ochoa, J. R.
Zaykowski, J. J.

ELECTRO-OPTICAL MATERIALS AND DEVICES

B. Y. Tsaur, *Leader*
D. L. Spears, *Assistant Leader*
R. C. Williamson, *Senior Staff*

Bailey, R. J.
Betts, G. E.
Choi, H. K.
Choi, S. S.*
Connors, M. K.
Cronin, S.*
Donnelly, J. P.
Goodhue, W. D.
Harman, T. C.

Liau, Z. L.
Manfra, M. J.
Missaggia, L. J.
Mull, D. E.
Napoleone, A.
Nee, P.*
Nitishin, P. M.
Oakley, D. C.
O'Donnell, F. J.

Poillucci, R. J.
Reeder, R. E.
Rossler, J. M.*
Royter, Y.*
Turner, G. W.
Vineis, C. J.*
Walpole, J. N.
Wang, C. A.

*Research Assistant

[†]Intergovernmental Personnel Act assignment

HIGH SPEED ELECTRONICS

M. A. Hollis, *Leader*
E. R. Brown, *Assistant Leader*[†]

Bozler, C. O. McIntosh, K. A.
Calawa, A. R.‡ McMahon, O. B.
Calawa, S. D. Molnar, R. J.
Chen, C. L. Parameswaran, L.
Graves, C. A. Rabe, S.
Harris, C. T. Rathman, D. D.
Lightfoot, A. Verghese, S.
Mahoney, L. J. Young, A. M.
Mathews, R. H.

ANALOG DEVICE TECHNOLOGY

T. C. L. G. Sollner, *Leader*
L. M. Johnson, *Assistant Leader*
A. C. Anderson, *Senior Staff*

Ala'ilima, T. F. Macedo, E. M., Jr.
Arsenault, D. R. McClure, D. W.
Berggren, K. Murphy, P. G.
Boisvert, R. R. Oates, D. E.
Feld, D. A. Sage, J. P.
Fitch, G. L. Santiago, D. D.
Hamm, J. M. Seaver, M. M.
Holtham, J. H. Slattery, R. L.
Lyons, W. G.

MICROELECTRONICS

E. D. Savoye, *Leader*
B. B. Kosicki, *Associate Leader*
B. B. Burke, *Senior Staff*

Aull, B. F. Hotaling, T. C.
Cooper, M. J. Johnson, K. F.
Daniels, P. J. Lind, T. A.
Doherty, C. L., Jr. Loomis, A. H.
Dolat, V. S. McGonagle, W. H.
Donahue, T. C. Percival, K. A.
Felton, B. J. Reich, R. K.
Gregory, J. A. Young, D. J.

ADVANCED SILICON TECHNOLOGY

C. L. Keast, *Leader*
P. W. Wyatt, *Associate Leader*

Berger, R. Knecht, J. M.
Burns, J. A. Liu, H. I.
Chen, C. K. Newcomb, K. L.
Davis, P. V. Sexton, S. V.
D'Onofrio, R. P. Soares, A. M.
Frankel, R. S. Suntharalingam, V.
Fritze, M. Young, G. R.

‡Part Time

†Intergovernmental Personnel Act assignment

1. QUANTUM ELECTRONICS

1.1 OPTICALLY PUMPED MID-INFRARED SEMICONDUCTOR LASER TECHNOLOGY FOR INFRARED COUNTERMEASURES

A compact, Stirling-cooled, 4- μm semiconductor laser package prototype using GaSb-based semiconductor materials and double heterostructure designs has been built and used in field tests. The package employed two broad-area diode-pumped semiconductor lasers that were polarization multiplexed to increase the power and brightness. InGaAs diode lasers operating near 1 μm were used as the pump source. The output power as a function of pump power of one of the two lasers is shown in Figure 1-1 for a heatsink temperature of 72 K at different pulse lengths. The drop in power for longer pulses occurs because of heating of the semiconductor gain element during the pulse. Higher power could be generated at lower heatsink temperature and with shorter pulses. At 40 K, the maximum combined peak power of both lasers was 3.5 W at 100- μs pulse length and 2.5-kHz pulse repetition frequency. A beam conditioner was used to shape the asymmetric beam output into a nearly symmetric profile in both near and far field. The beam conditioner included a cylindrical beam expander and a multiple-reflection beam segmenter consisting of two mirrors. In the field, a 2-in.-aperture telescope was used to further narrow the far field,

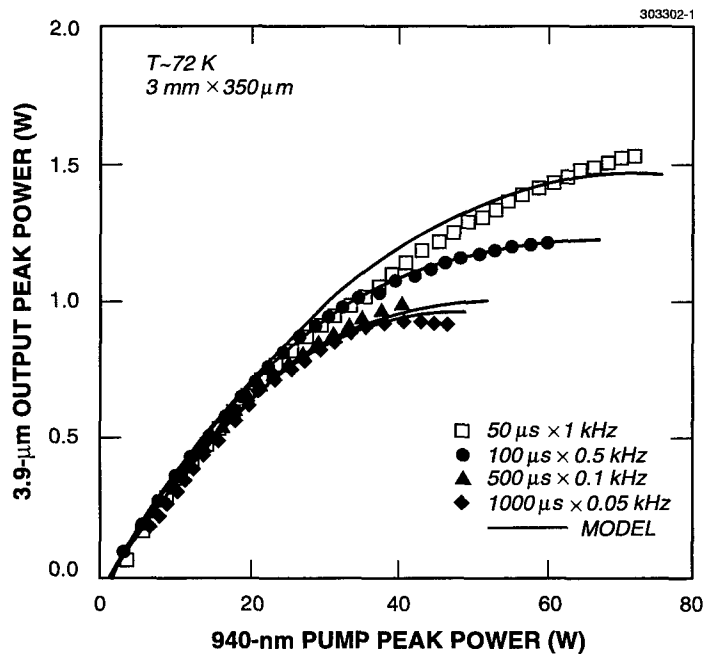


Figure 1-1. Power output of broad-area InAsSb double-heterostructure laser.

and 40% of the power was within 1 mrad. The optical transmission through the polarization beam combiner and the beam conditioner was only 50% because of beam clipping and nonoptimal optical coatings; better optics should allow ~90% transmission.

The mode of operation of the laser is dictated by the finite cooling capacity of the Stirling cooler, because the optical-to-optical efficiency of the lasers decreases as the temperature of the semiconductor gain element increases. The laser was typically operated at a low power level to avoid the inefficiency regime near the thermal roll-off. Shown in Figure 1-2 is an example of burst mode of operation with a 10-s ON-period followed by a 300-s OFF-period. It is clear that package output was stabilized after ~4 cycles. In the field, the package was operated at 1.1-W peak power in 0.5-ms pulses at 25% duty cycle (0.28-W average).

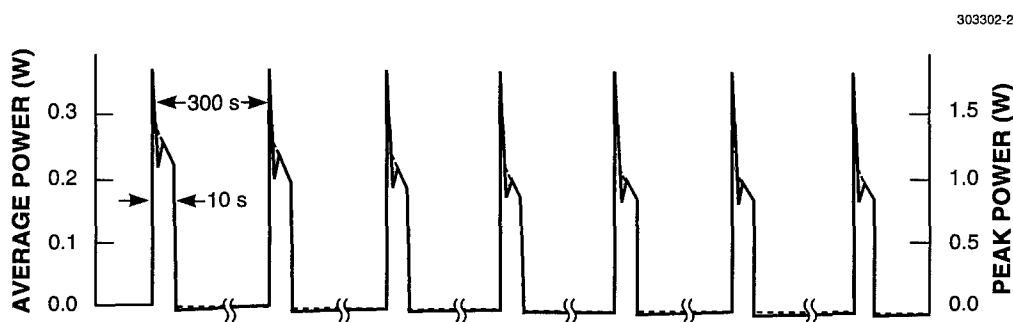


Figure 1-2. Power output from the Stirling cooler package shown in Figure 1-1. Solid and dashed lines are experiment and model, respectively. Oscillation and overshoot in the data are due to the power meter response. The pulse length is 100 μ s and the pulse repetition frequency is 2 kHz.

Besides the compact package, other liquid-N₂-cooled 4- μ m lasers have been built for laboratory use. One unit provided 0.2 W cw with a 20 times diffraction limited beam. Other pulse units have operated in a long-pulse mode (hundreds of microseconds, 0.4-W peak) or a short-pulse mode (tens of nanoseconds, 8-W peak). All of these devices have been pumped near 1 μ m.

Based on the performance of the prototypes, extrapolation to a future package can be done. The key elements for a better laser package are higher cooling capacity, more efficient optics, better beam quality, and higher-efficiency devices. For example, pumping at 2 μ m improves the optical efficiency while reducing the thermal load in the gain element. The incremental improvement of each of these factors on the package overall brightness is determined using computer simulation.

H. Q. Le	T. Y. Fan
G. W. Turner	D. L. Spears
H. K. Choi	A. Sanchez
V. Daneu	

2. ELECTRO-OPTICAL MATERIALS AND DEVICES

2.1 MICRON-SIZE LARGE-NUMERICAL-APERTURE MICROLENSES IN GaP FABRICATED BY MASS-TRANSPORT SMOOTHING OF ETCHED SINGLE MESAS

Interest in large-numerical-aperture microoptics has been considerable, especially for semiconductor laser and optical interconnection applications. While most microlenses developed to date are of aperture sizes of a few hundred microns, smaller micron-size ones can be placed very close to the laser facets for special beam shaping and compact packaging. The recent mass-transport technique is potentially suitable for fabricating small lenses [1]–[3]. However, the micron-size profiles would be too small for the conventional multimesa preform approaches. In this work, an alternative approach is proposed, which utilizes the naturally curved surfaces in the mass-transport smoothing of single mesas. We show that the surface profiles can be accurately tailored by controlling the mesa dimensions and the mass-transport kinetics.

Periodically repeated mesas are presented here (see Figure 2-1) because of the simplicity provided by the use of Fourier series, although Fourier integrals have been used to treat isolated single mesas. By symmetry, rectangular mesas with equal width and separation (see the dotted curve in Figure 2-1) can be represented by a Fourier cosine series with only odd-numbered terms,

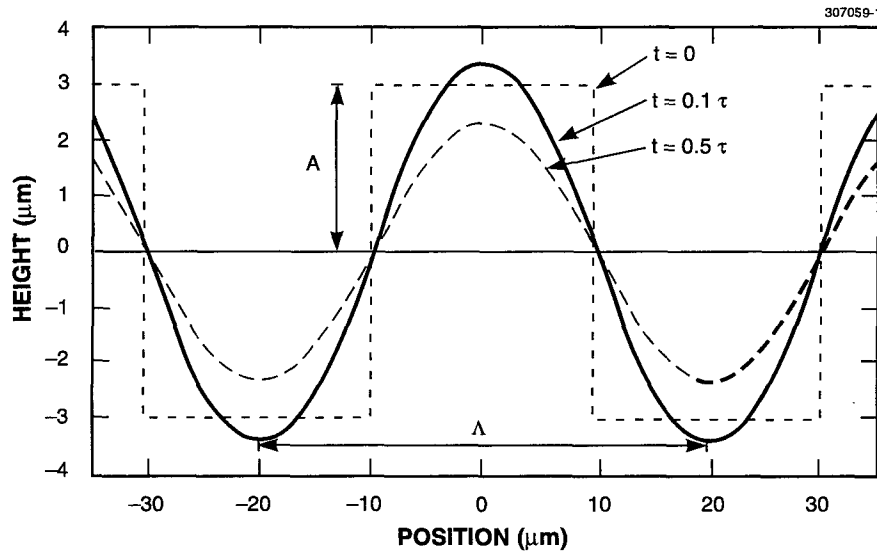


Figure 2-1. Mass-transport smoothing of periodic array of etched mesas. After a relatively short mass-transport time ($t = 0.1\tau$) the profile is more spherical near the center and can better approximate a desired lens profile. After a longer time ($t = 0.5\tau$), the profile becomes purely sinusoidal.

$$z(x,0) = \frac{4A}{\pi} \cos \frac{2\pi x}{\Lambda} - \frac{4A}{3\pi} \cos \frac{6\pi x}{\Lambda} + \dots, \quad (2.1)$$

where z is the height, x is the position, A is half of the initial mesa height, and Λ is the fundamental spatial wavelength.

When the structure is subjected to a heat treatment, the profile undergoes a transformation because of the surface energy and mass transport, and according to earlier models [4]–[6]

$$z(x,t) = \frac{4A}{\pi} e^{-t/\tau} \cos \frac{2\pi x}{\Lambda} - \frac{4A}{3\pi} e^{-27t/\tau} \cos \frac{6\pi x}{\Lambda} + \dots, \quad (2.2)$$

where t is the mass-transport time and τ is the decay lifetime of the fundamental term. In defining Equation (2.2), a vapor-transport process has been assumed in which $\tau = \tau_0(\Lambda/\Lambda_0)^3$, where τ_0 and Λ_0 are parameters which characterize the mass-transport process. (For the surface-diffusion regime, a fourth-power dependence should be used.) Also note that, because of the strong spatial wavelength dependence, the higher-order terms decay much more rapidly, eventually leaving just the fundamental term, i.e.,

$$z(x,t) \approx \frac{4A}{\pi} e^{-t/\tau} \cos \frac{2\pi x}{\Lambda}, \quad (2.3)$$

as illustrated in Figure 2-1.

In practice, the mass-transport time is usually fixed at a given value, and the condition of Equation (2.3) can be reached when the fundamental spatial wavelength Λ (and hence the decay lifetime τ) is not too large. The radius of curvature near the center of such a sinusoidal (cosine) profile is then given by

$$\begin{aligned} R &= \left(\frac{\partial^2 z}{\partial x^2} \right)^{-1}_{x=0} \\ &= \frac{\Lambda^2}{16\pi A} e^{t/\tau}, \end{aligned} \quad (2.4)$$

which can be varied (by properly choosing the amplitude A) to approximate any lens profile.

However, especially for large-numerical-aperture lenses, the approximate profile can deviate considerably from the ideal one in regions away from the center. To increase the useful aperture, better approximation can be obtained by retaining the next higher order term in the Fourier expansion by the use of a somewhat larger Λ . A simple rule for the improvement is to match not only the second but also the fourth derivatives of the ideal profile, b and c , respectively, i.e.,

$$\left. \frac{\partial^2 z}{\partial x^2} \right|_{x=0} = -\frac{4A}{\pi} \left(\frac{2\pi}{\Lambda} \right)^2 \left(e^{-t/\tau} - 3e^{-27t/\tau} \right) = b \quad (2.5)$$

and

$$\left. \frac{\partial^4 z}{\partial x^4} \right|_{x=0} = \frac{4A}{\pi} \left(\frac{2\pi}{\Lambda} \right)^4 \left(e^{-t/\tau} - 27e^{-27t/\tau} \right) = c . \quad (2.6)$$

Since τ is related to Λ , i.e., $\tau = \tau_0(\Lambda/\Lambda_0)^3$, with references τ_0 and Λ_0 available from calibration runs, Equations (2.5) and (2.6) can readily be solved for the two unknowns Λ and A by using the following procedure. A division between the two equations yields

$$\left(\frac{2\pi}{\Lambda} \right)^2 \frac{e^{-t/\tau} - 27e^{-27t/\tau}}{e^{-t/\tau} - 3e^{-27t/\tau}} = -\frac{c}{b} , \quad (2.7)$$

from which a solution for Λ can be found graphically. Then, by plugging Λ back into Equation (2.5), A can be evaluated.

As a numerical example, the above Fourier expansion technique will now be used to approximate a concave spherical profile

$$z = R - \sqrt{R^2 - x^2} , \quad (2.8)$$

where R is the constant radius of curvature, and $R = 14 \mu\text{m}$, relevant to an actual diode laser application, is chosen. It can then be readily shown that

$$b = 1/R = 0.07143 \quad (2.9)$$

and

$$c = 3/R^3 = 0.00109 . \quad (2.10)$$

Experimental values of $\tau_0 = 3 \text{ h}$ at $\Lambda = 10 \mu\text{m}$ (at $T = 1100^\circ\text{C}$), and $t = 24 \text{ h}$ are also adopted. Equations (2.5) and (2.6) then yield $\Lambda = 41.78 \mu\text{m}$ and $A = -3.348 \mu\text{m}$. These values are subsequently plugged into Equation (2.1) for the approximate profile. As shown in Figure 2-2, the profile agrees with the ideal one over an aperture size of nearly $11 \mu\text{m}$, where the deviations are less than a tolerable 20 nm . Note that, with $R = 14 \mu\text{m}$ and $n = 3.1$ (GaP), the aperture size corresponds to a large numerical aperture of 0.73. In fact, even larger apertures can be achieved by using somewhat more sophisticated fitting schemes. For example, one can implement a somewhat larger fourth derivative to slightly raise the approximate profile in order to better match the ideal one over a larger aperture, so long as a sufficiently small overall mean-square deviation is maintained.

In contrast, the simplest sinusoidal profile, as given by Equations (2.3) and (2.4), results in a smaller useful aperture, as illustrated by the lower curve in Figure 2-2.

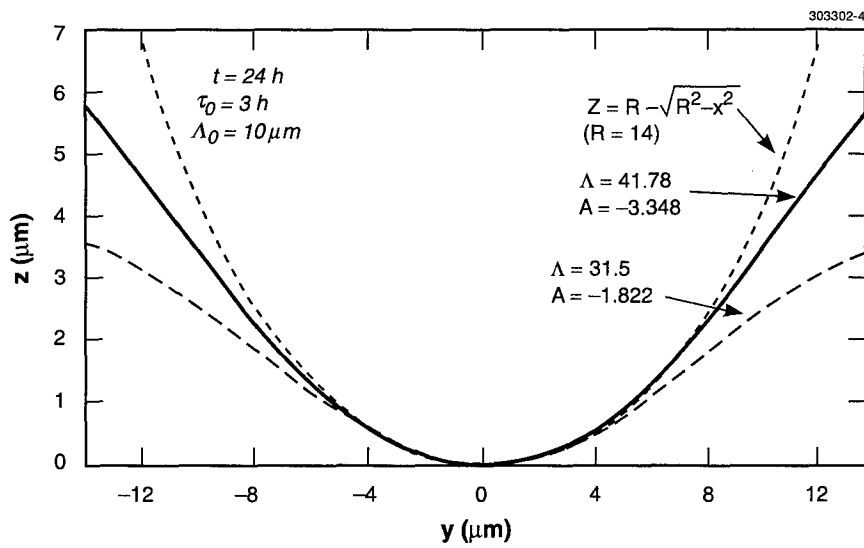


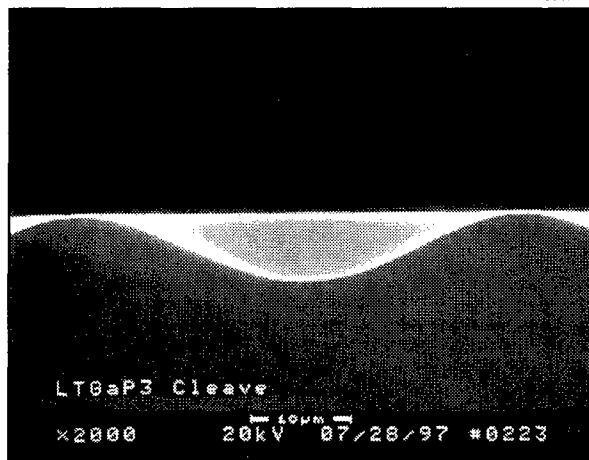
Figure 2-2. Approximation of micron-size spherical profile by mass-transport smoothing of etched mesa. By choosing suitable mesa width and height, $\Lambda/2$ and $2A$, respectively, for a given mass-transport temperature and time, the spherical profile is well approximated over a useful large aperture.

The scanning electron microscope photographs in Figure 2-3 show an initial experimental result. These are cleaved cross-sectional views of a concave cylindrical lens formed by mass-transport smoothing of etched mesas in a GaP substrate. Note that a smooth, nearly sinusoidal profile has been obtained, as shown in Figure 2-3(a), and a nearly ideal lens profile has been formed near the center, as shown in Figure 2-3(b). Measurements on Figure 2-3(b) showed a nearly constant radius of curvature over an aperture size of $12 \mu\text{m}$, in agreement with the model.

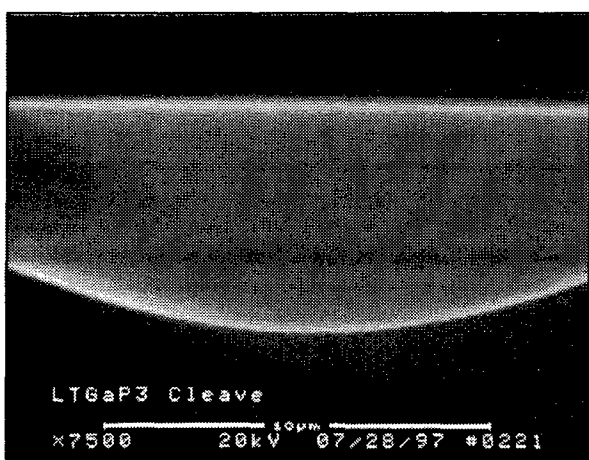
Z. L. Liau J. D. Woodhouse*
 L. A. Scheffel* P. S. Whitney*
 D. C. Flanders*

*Author not at Lincoln Laboratory.

306487-1L



(a)



(b)

Figure 2-3. Scanning electron micrograph of cleaved cross section of fabricated GaP cylindrical microlens: (a) is lower magnification showing the nearly sinusoidal profile formed by a smoothing of etched rectangular mesas, and (b) shows a higher magnification near the center where a nearly constant curvature has been measured.

2.2 HIGH-POWER 1.5- μ m InGaAsP/InP LASERS WITH A TAPERED GAIN REGION

Semiconductor lasers and amplifiers with tapered gain regions are well suited for applications requiring high output powers and good spatial mode quality. Operation of these large-area devices requires epitaxial material with excellent uniformity. GaAs-based devices have been well demonstrated and we have recently reported InGaAsP/InP tapered lasers and amplifiers that operate at $\lambda \approx 1.3 \mu\text{m}$ [7]–[8]. In this report, the development of 1.5- μm InGaAsP/InP quantum-well material suitable for this type of device is discussed, and initial results on high-power tapered lasers with near-diffraction-limited beam widths fabricated in this material are presented.

Several different 1.5- μm quantum-well laser structures, grown by organometallic vapor-phase epitaxy in an atmospheric-pressure chimney reactor, are being evaluated for this application. Details of the different laser structures and epitaxial growth can be found in Ref. 9. Here, results are presented for devices fabricated in a two-step separate-confinement heterostructure (SCH) with three 8-nm-thick quantum wells under 1% biaxial compression. As characterized by broad-area laser measurements, this material has a transparency current density $J_0 \approx 190 \text{ A/cm}^2$ and a net modal gain (gain- α) of $\sim 40 \text{ cm}^{-1}$ at $\sim 1000 \text{ A/cm}^2$.

The tapered device structure used here is illustrated in Figure 2-4. It has a single-mode ridge-waveguide input gain section coupled to a tapered gain region. The tapered gain region is defined by the taper contact which has a cone angle of $\sim 6^\circ$. Devices with a 1-mm-long ridge input section and either

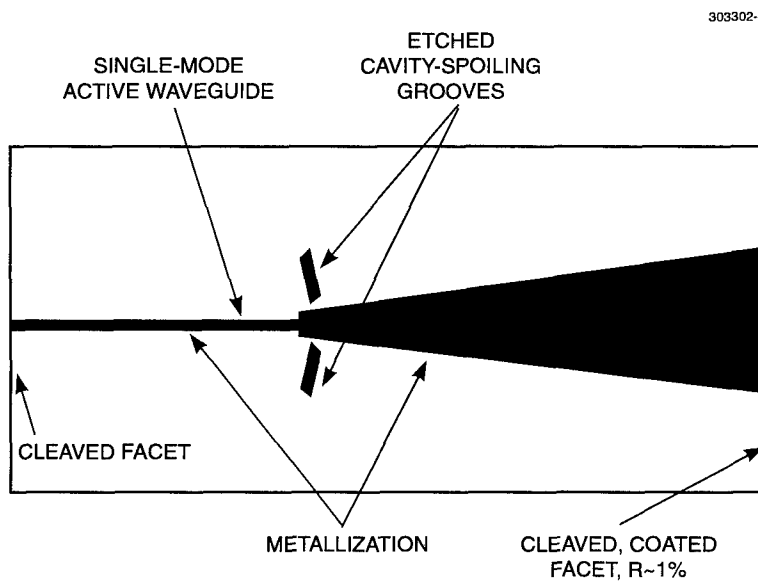


Figure 2-4. Device design for 1.5- μm tapered lasers.

1- or 2-mm-long taper sections were fabricated and evaluated. The cw output power vs current of a device with a 2-mm-long taper region and a 210- μm output aperture, which was coated to have a reflectivity of ~1%, is shown in Figure 2-5. The threshold current is 1.1 A, and 0.9 W of output power is obtained at 4 A. The far-field pattern in the plane of the junction of this device operating at 4 A is shown in Figure 2-6. About 80% of the 0.9-W output is in the near-diffraction-limited central lobe of the far-field pattern. Devices with a 1-mm-long taper region had cw output powers of 0.5 W at 2.5 A, of which 86% was in the central lobe of the far-field pattern.

Tapered devices are currently being fabricated in stepped-graded-index SCH material [3], which has slightly lower J_0 and higher differential gain (net gain $> 40 \text{ cm}^{-1}$ at $< 800 \text{ A/cm}^2$) than comparable two-step SCH material. Devices are also being fabricated in five-quantum-well material to investigate the effects of the number of quantum wells on threshold current, efficiency, output power, and output beam quality.

J. P. Donnelly J. N. Walpole
S. H. Groves R. J. Bailey

REFERENCES

1. Z. L. Liau, V. Diadiuk, J. N. Walpole, and D. E. Mull, *Appl. Phys. Lett.* **52**, 1859 (1988); **55**, 97 (1989).
2. Z. L. Liau, D. E. Mull, C. L. Dennis, R. C. Williamson, and R. G. Waarts, *Appl. Phys. Lett.* **64**, 1484 (1994).
3. J. S. Swenson, Jr., R. A. Fields, and M. H. Abraham, *Appl. Phys. Lett.* **66**, 1304 (1995).
4. W. W. Mullins, *J. Appl. Phys.* **30**, 77 (1959).
5. Z. L. Liau and H. J. Zeiger, *J. Appl. Phys.* **67**, 2434 (1990).
6. Z. L. Liau, *Mater. Chem. Phys.* **46**, 265 (1996).
7. J. N. Walpole, J. P. Donnelly, S. H. Groves, L. J. Missaggia, J. D. Woodhouse, R. J. Bailey, and A. Napoleone, *IEEE Photon. Technol. Lett.* **8**, 1450 (1996).
8. J. P. Donnelly, J. N. Walpole, G. E. Betts, S. H. Groves, J. D. Woodhouse, F. J. O'Donnell, L. J. Missaggia, R. J. Bailey, and A. Napoleone, *IEEE Photon. Technol. Lett.* **8**, 1429 (1996).
9. Solid State Research Report, Lincoln Laboratory, MIT, 1997:1, p. 5.

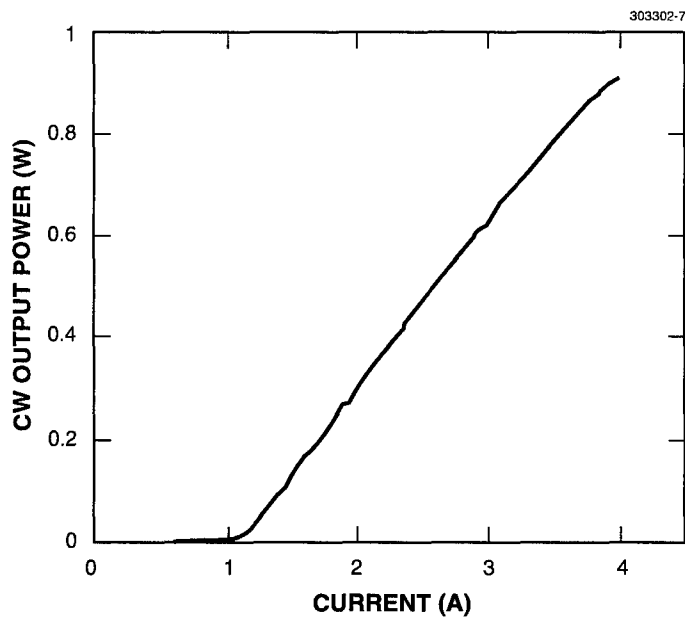


Figure 2-5. CW output power vs current for 1.5- μm tapered laser with 1-mm-long ridge input section and 2-mm-long tapered section.

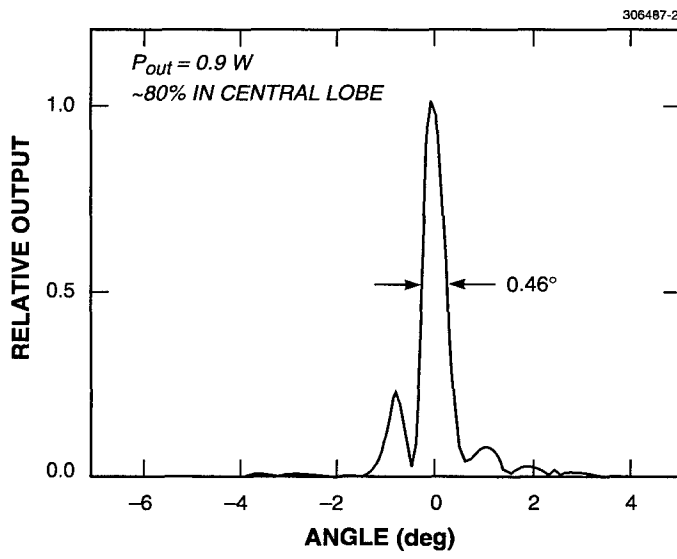


Figure 2-6. Beam profile in plane of the junction of tapered laser oscillator with 0.9-W cw output.

3. SUBMICROMETER TECHNOLOGY

3.1 OPTICAL LITHOGRAPHY WITH 157-nm LASERS

Projection photolithography at 157 nm was evaluated as a possible extension of current 248-nm and planned 193-nm technologies. The traditional scaling laws of resolution and depth of focus with wavelength indicate that it will be worthwhile to change to 157-nm lithography to increase process latitude for 0.13- μm and smaller features. This can be confirmed using aerial image simulations as summarized in Figure 3-1 for the case of equal lines and spaces. Similar analyses have been performed for unequal lines and spaces, with similar conclusions.

A major consideration in the selection of the 157-nm exposure wavelength is the availability of high-quality F₂ laser sources. These lasers use a mixture of 5% fluorine in helium and pure helium, in a ratio of 1:40, at a total pressure of 3200 mbar. Typical operating conditions are 35 mJ/pulse at 200 Hz, and the pulse-to-pulse energy stability is within 10%. The output spectrum of a F₂ laser is considerably narrower than that of an ArF or KrF laser. The 193- and 248-nm emissions in the latter correspond to bound-to-dissociative state transitions, and are therefore 200–300 pm broad. The 157-nm emission, on the other hand, corresponds to several discrete rotational-vibrational transitions. The most detailed output spectrum of a F₂ laser is reported in Ref. 1. Its full width at half-maximum is only ~17 pm, which can have important implications for catadioptric projection systems, which even at relatively high numerical apertures may not require further line narrowing.

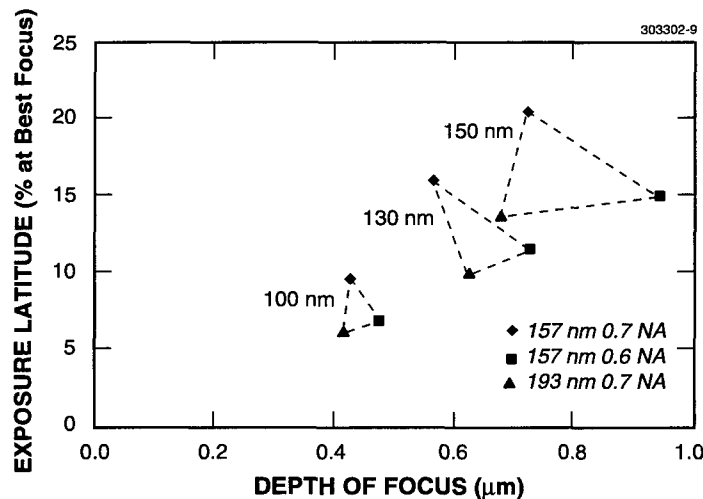


Figure 3-1. Comparison of depth of focus at best dose and exposure latitude at best focus, as calculated from aerial image simulations. The printed features are equal lines and spaces, at the dimensions indicated (100, 130, and 150 nm). The imaging configurations are 193 nm at 0.7 numerical aperture (NA), and 157 nm at 0.6 and 0.7 NA, all three with circular illumination and spatial coherence 0.6.

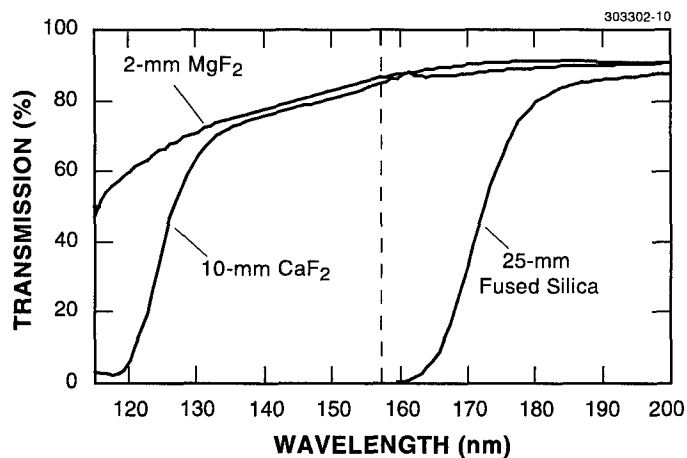


Figure 3-2. Measured transmission of fused silica, crystalline calcium fluoride, and crystalline magnesium fluoride, at the respective indicated thicknesses. The broken vertical line indicates the 157-nm wavelength.

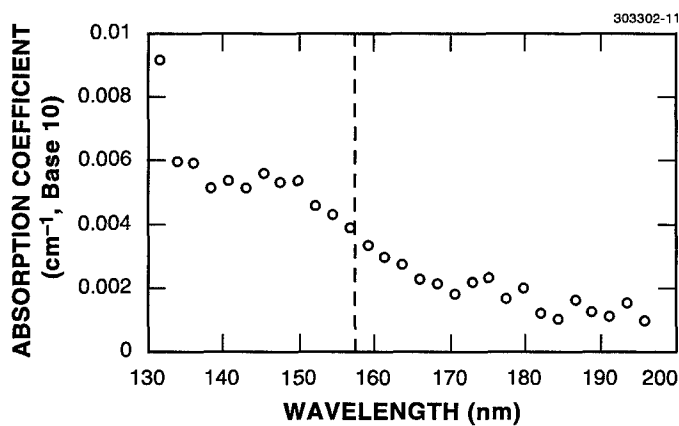


Figure 3-3. Absorption coefficient of calcium fluoride in the range 130–200 nm, as calculated from transmission measurements performed with a vacuum uv spectrophotometer on three prism-shaped samples along their 10- and 40-mm axes, as described in the text. At 157 nm the absorption coefficient is $\sim 0.004 \text{ cm}^{-1}$. The broken vertical line indicates the 157-nm wavelength.

The greatest area of concern in 157-nm lithography is the availability of refractive optical materials suitable for all-refractive or catadioptric designs. As Figure 3-2 indicates, fused silica is semiopaque at this wavelength, and only a few crystalline fluorides are acceptable candidates. Of these, MgF₂ is birefringent, and LiF is too soft and hygroscopic. High-purity, crystalline CaF₂ is probably the only choice, and therefore its properties must be evaluated carefully.

We have performed several experiments in which the transmission of three samples was measured in a vacuum uv spectrophotometer, and also directly with the 157-nm laser. Each sample was a rectangular prism, with dimensions 10 × 20 × 40 mm, and all six sides were polished. By measuring the transmission along different lengths of the same samples, the bulk absorption coefficient could be calculated and separated from surface losses. This methodology was important, because surface attenuation of 3–4%/surface is seen at 157 nm in the spectrophotometer, whereas bulk transmission losses are only ~1%/cm. Figure 3-3 shows the wavelength-dependent bulk absorption coefficient k , as determined from the spectrophotometer measurements. The absorption coefficient is related to the transmission T by

$$T = (1 - R)^2 (1 - 2f_s) e^{-2.3kL} \cdot \frac{1}{1 - R^2 (1 - 4f_s) e^{-4.6kL}} , \quad (3.1)$$

where L is the sample length, R is the reflection coefficient, and f_s represents surface losses. At 157 nm we have measured $k \approx 0.004 \text{ cm}^{-1}$, both with the spectrophotometer and with the laser.

In order to assess the significance of this value, it is illustrative to compare the thermal budget of CaF₂ at 157 nm to that of fused silica at 193 nm. The important quantities are the thermal coefficient of the refractive index dn/dT , the thermal coefficient of expansion $(dL/L)/dT$, and the thermal conductivity K . The temperature rise induced by absorption of laser power is inversely proportional to K . Also, the fractional change in optical path with temperature OPD/dT is given by

$$OPD/dT = [(n - 1)/n](dL/L)/dT + (1/n)dn/dT . \quad (3.2)$$

Table 3-1 lists the relevant parameters for CaF₂ and fused silica. Note that, since its K is ~7 times larger than that of fused silica, CaF₂ can accommodate a proportionately higher absorption. This trend is compounded by the ~1.6 times weaker dependence of OPD on temperature in CaF₂ than in fused silica. Thus, an order of magnitude higher absorption coefficient k can be accommodated by CaF₂ at 157 nm than by fused silica at 193 nm. As a point of reference, the best grades of fused silica have been measured to have $k \sim 0.002 \text{ cm}^{-1}$. Thus, the value of $k \sim 0.004 \text{ cm}^{-1}$ that we have measured for CaF₂ at 157 nm is well within the acceptable range.

TABLE 3-1
Optical and Physical Material Parameters at 157 and 193 nm

	CaF₂ 157 nm	CaF₂ 193 nm	Fused Silica 193 nm
Refractive index (Refs. 2, 3)	1.56	1.50	1.56
dn/dT (ppm/°K) (Refs. 2, 4)	3.0	-5.9	22
$(dL/L)/dT$ (ppm/°K) (Refs. 5, 6)	19	19	0.52
OPD/dT (ppm/°K) [Equation (3)]	8.7	2.4	14
Thermal conductivity K (W/m°K) (Ref. 7)	9.7	9.7	1.4

The measured surface losses mentioned above, ~3%/surface in the spectrophotometer, are smaller in the laser beam. This effect leads us to postulate that they are due to incomplete surface cleaning or to adsorbates from the ambient. Further studies are under way to identify the exact mechanism.

The long-term durability of CaF₂ is another area of concern. To date, we have irradiated three samples at 5–8 mJ/cm²/pulse for 25 million pulses, and have found no detectable changes in transmission at 157 nm. The only reported color centers in CaF₂ are at 360 nm and at longer wavelengths, so our results are not surprising. Nevertheless, we plan to continue marathon irradiation of CaF₂ at 157 nm, and will monitor any changes in its transmission.

In general, the use of a new exposure wavelength will require the development of new resist systems. However, we have demonstrated that the positive-tone silylation process of polyvinylphenol, which exhibits a large process window at 193 nm [8], is directly transferable to 157 nm. Figure 3-4 shows that the effect of 157-nm irradiation on silylation efficiency is nearly identical to that of 193 nm, provided the exposures are performed in the same ambient (nitrogen). Here, the silicon uptake, as measured by Fourier transform infrared spectroscopy of the Si-O-CH_x peak in the film, is plotted as a function of the exposure dose. Specifically, the inhibition of silylation begins at ~10 mJ/cm², and is nearly complete at ~80 mJ/cm².

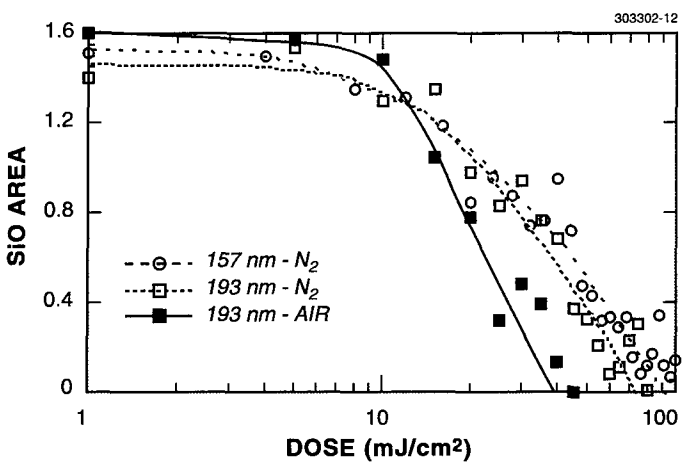


Figure 3-4. Silicon uptake in the vapor phase silylation of polyvinylphenol as a function of exposure dose at 157 nm (in nitrogen) and 193 nm (in nitrogen and in air). The silylation efficiency is determined by the area under the Si-O-CH_x absorption band measured with a Fourier transform infrared spectrophotometer. Exposure in nitrogen has almost the same effect at the two wavelengths, and is markedly less efficient than 193-nm exposure in air in suppressing silylation.

A simple exposure system has been constructed to demonstrate the resolution achievable using 157-nm lithography. The projection optics consists of an all-reflective Schwarzschild 36 \times objective with 0.50 numerical aperture (NA). Since oxygen and water vapor are strong absorbers at 157 nm [9], care has been taken to efficiently purge the beam line with filtered nitrogen from the laser through the reticle and the projection optics. Only a ~2-mm gap exists between the optics housing and the wafer, and at typical nitrogen flow rates of ~10 sccm the gap is sufficiently flooded that no measurable attenuation of laser energy is observed. At 157 nm, conventional fused silica reticles would be too absorbing. We have developed a chrome-on- CaF_2 reticle technology using a ~20-nm-thick chrome layer that is deposited by electron beam evaporation and etched by argon ion beam milling. We have also developed a chromeless phase-shifting CaF_2 mask technology. In this case ion beam milling is used to etch 135-nm-high steps, which correspond to a phase shift of half a wavelength, directly into the CaF_2 substrate.

This experimental system has been used to pattern polyvinylphenol resist films. The 0.3- μm -thick films were exposed at a fluence of 1 $\text{mJ}/\text{cm}^2/\text{pulse}$ and a total dose of ~50 mJ/cm^2 . Silylation was performed with dimethylsilyldimethylamine at 10 Torr for 30 s at 100°C, followed by etching in an oxygen plasma in a parallel-plate reactive ion etcher. Figure 3-5 shows the high-resolution images obtained by combining the phase-shifting mask with the 0.5-NA optics. The printed features, 80-nm lines, correspond

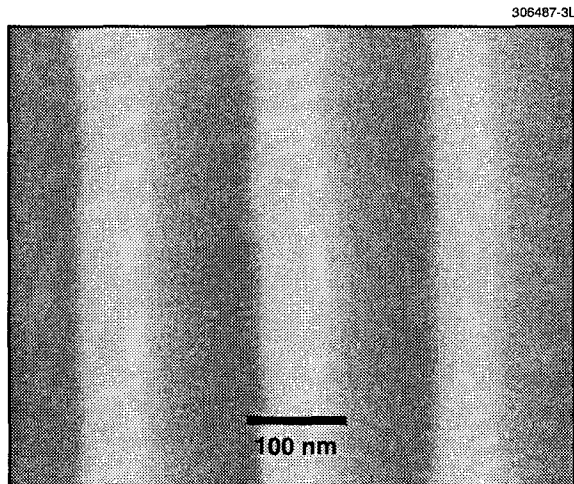


Figure 3-5. Scanning electron micrograph of 80-nm lines printed in projection at 157 nm with 0.5-NA objective. The resist process was top-surface imaging in polyvinylphenol, followed by vapor phase silylation and oxygen reactive ion etching. The mask was a 36 \times chromeless edge shifter, fabricated in calcium fluoride.

to the limit of this method, namely $0.25 \lambda/\text{NA}$. These are, we believe, the smallest features printed to date using optical projection lithography.

T. M. Bloomstein	R. R. Kunz
M. W. Horn	S. T. Palmacci
M. Rothschild	R. B. Goodman

3.2 NEW SURFACE EMISSION CATHODE IN DIAMOND

Many groups have reported excellent electron emission from diamond and amorphous diamond-like films, yet practical application of these cathodes has been limited by a serious lack of reproducibility [10],[11]. Electron emission typically appears to originate from a relatively small number of spatially localized sites, and this is generally believed to be due to the inconsistent bulk properties of the deposited carbon-based cathode material. Enhanced electron emission at the triple junction interface between the diamond surface, a conductive region, and vacuum is a newly proposed emission mechanism that may help explain the localization of emission sites [12].

A triple junction [13],[14] is the intersection of an insulator or semiconductor surface with a metal substrate in vacuum. When an electric field along this insulating surface is produced by a negative bias on the metal substrate, a substantial positive charge can form on the surface and in the bulk of the semiconductor near the triple junction. Part of this charge is the result of the Schottky diode the semiconductor forms with the metal substrate. In addition, if the field is large enough, electrons will tunnel from the metal substrate onto the semiconducting surface with sufficient energy to cause secondary electron emission, which will further increase this positive charge. The electric field enhancement is dependent upon the angle the semiconductor-vacuum interface makes with the metal substrate, shown in Figure 3-6 as Θ . The surface emission cathode exploits this electric field enhancement combined with the high electron mobility on the interface between the negative electron affinity (NEA) semiconductor surface and vacuum to form a high-performance electron emitter.

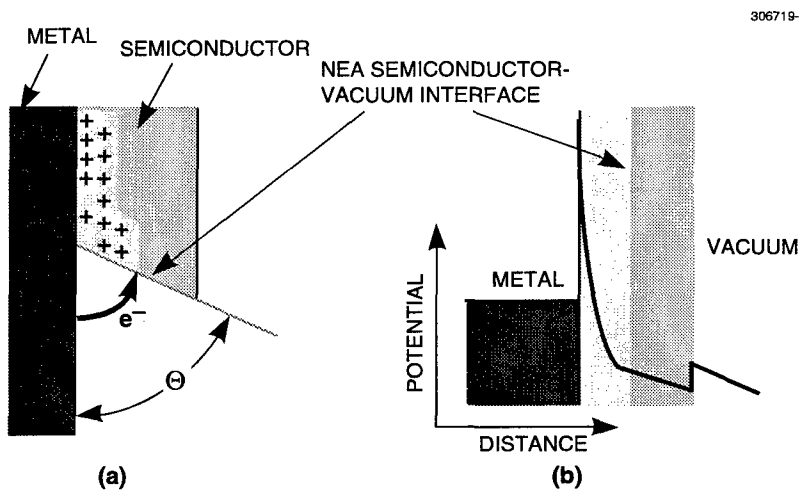


Figure 3-6. Triple junction (metal-NEA semiconductor-vacuum) electric field enhancement cathode: (a) shows a cross section of a triple junction formed by the metal-NEA semiconductor-vacuum interface. The lighter region in the semiconductor near the metal-semiconductor interface is the space charge region containing the ionized dopants. (b) is a plot of potential energy along the NEA semiconductor-vacuum interface. Electrons tunnel from the metal substrate onto the NEA semiconductor-vacuum interface.

Initial experimental evidence for the surface emission phenomenon was provided by the simple experiment illustrated in Figure 3-7. A type Ib diamond, ~3 mm on a side, that contains substitutional nitrogen, a deep donor, was implanted with 34-keV Li^+ at 200°C to a dose of $4 \times 10^{16} \text{ cm}^{-2}$ to enhance the electrical contact between the metal support and the diamond [15],[16]. The anode, which could be moved from touching to several centimeters above the diamond, consisted of either a molybdenum rod 0.5 mm in diameter or a square phosphor screen ~1 cm on a side. The diamond was prepared for emission by exposing it to an O_2 discharge, coating it with Cs, and reexposing it to O_2 , a surface procedure known to

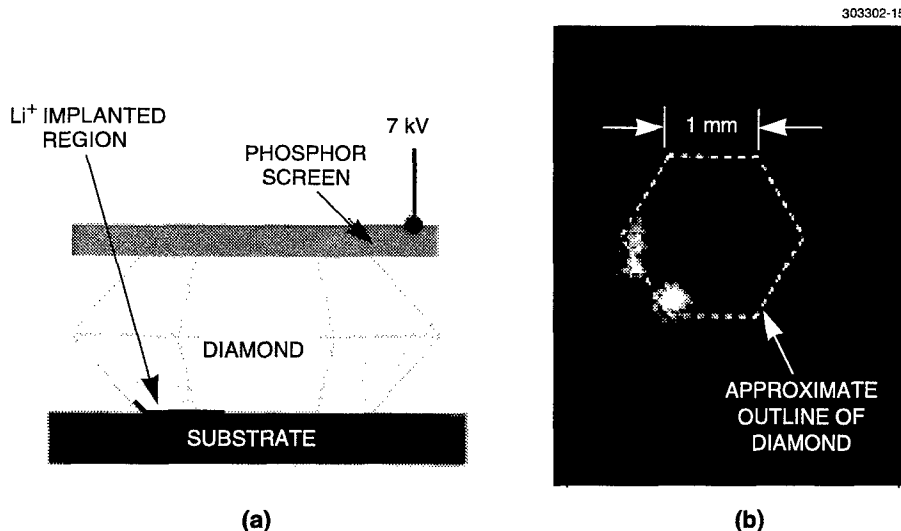


Figure 3-7. (a) Schematic diagram of Li^+ -implanted diamond with phosphor screen placed on top of the diamond. (b) Observed fluorescence of the phosphor screen. The fluorescence is directly under the portion of the diamond implanted with Li^+ . The screen continued to fluoresce when lifted several hundred micrometers above the diamond, but the fluorescing regions moved away from the edge of the diamond to its center and became more diffuse.

enhance diamond's NEA property [17],[18]. The anode was then positively biased until stable emission was obtained from the diamond, after which the vacuum electron emission from the top of the diamond appeared to originate from electrons that traveled across the diamond surface, rather than through its bulk. These electrons caused the surface of the diamond to glow green yellow. This glow originated from the ion-implanted region, up the side of the diamond, around the top edge, and then across the top surface. Surface irregularities caused variations in the path of the glowing regions. Once on the top surface, the electrons jump the 0–0.8-mm gap between the top diamond surface and the positively charged movable anode. When the anode was moved from touching the diamond to 0.5 mm above it, the anode voltage had to be increased by 12%, from 7 to 8 kV, to maintain a constant emission current of 1×10^{-5} A. This indicates that most of the potential drop, ~7 kV, appears across the diamond and is not being expended in the vacuum gap between the diamond and the anode [19]. When a phosphor screen was used as an anode and placed on the diamond surface, the screen fluoresced where it met the diamond, as shown in Figure 3-7. This screen will fluoresce only when hit with electrons of energy >1 keV, implying that these electrons have considerable energy while still on the diamond surface. We theorize that these electrons are field emitted from the implanted region into NEA semiconductor–vacuum surface states. Once in these states the electrons can be accelerated to high energies, >1 keV.

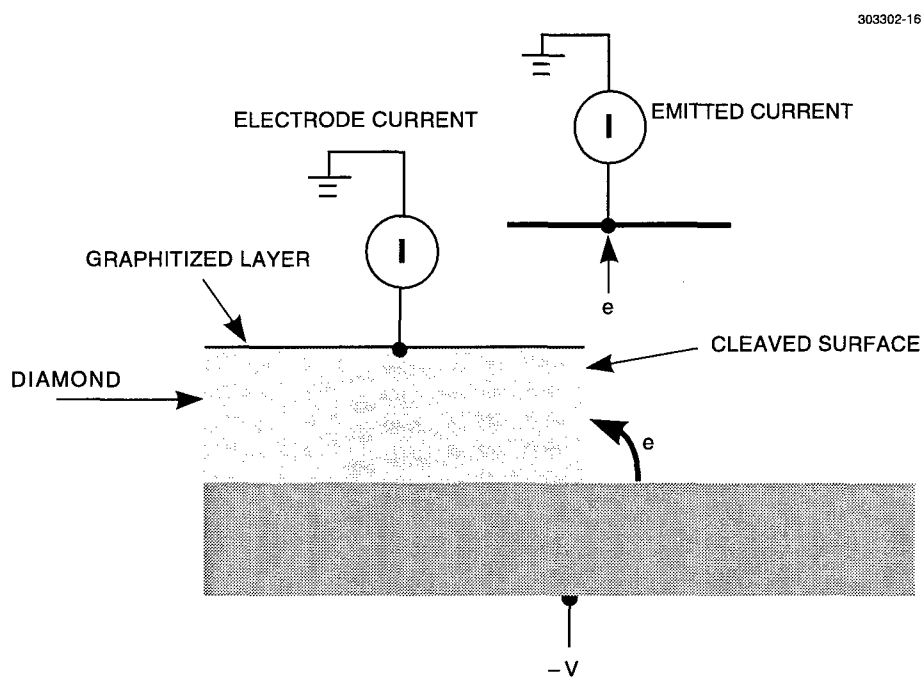


Figure 3-8. Schematic drawing of surface emission cathode experiment using the cleaved surface of diamond to emit electrons.

To further characterize the emission, a thinner, $100\text{-}\mu\text{m}$ -thick, type Ib diamond plate was coated on the back side with electron-beam-evaporated Ni and graphitized on the top to form a conductive layer. The graphite layer was formed by sputtering the diamond surface with 1200-eV Xe^+ . The diamond was then cleaved to obtain a clean, undamaged surface, as depicted in Figure 3-8. When a few kilovolts were placed between the Ni and graphitized layers, electrons were emitted into vacuum. This emission was further increased with the same $\text{O}_2\text{-Cs}$ treatment previously described. Figure 3-9 shows a typical result obtained from these surface emission cathodes. By using a movable phosphor screen it was determined that these electrons originated from the cleaved surface and appeared to form collimated beams. The apparatus shown in Figure 3-10 was then used to measure the energy of the emitted beam, and this experiment indicated that the electrons were nearly monoenergetic with energies within 50 eV of the applied potential.

The mechanism used to explain the surface emission relies upon positive charges at or near the diamond surface to create a large electric field at the triple junction, as depicted in Figure 3-6. This hypothesis was tested in the following experiment. We have found that nitrogen impurities in diamond can be positively ionized and remain charged for days, but once exposed to room light, photogenerated electrons in

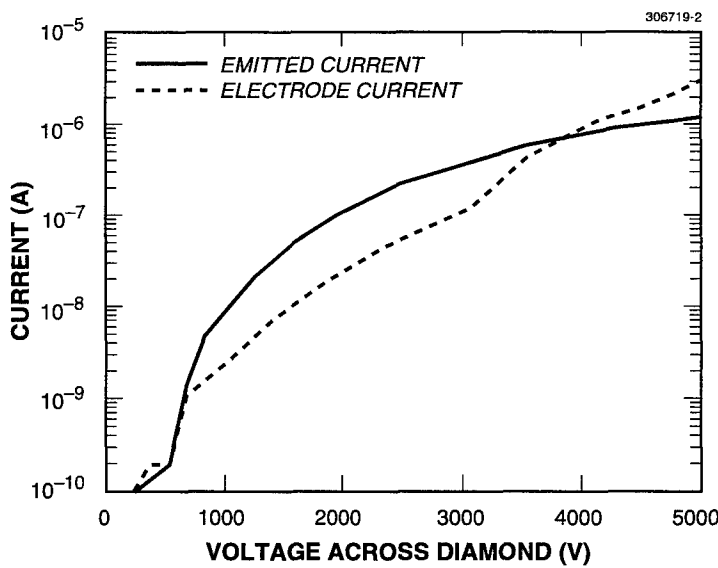


Figure 3-9. Plot of emitted and electrode currents as a function of applied voltage for the structure shown in Figure 3-8.

the diamond will neutralize the dopants. Figure 3-11 shows the effect of incandescent illumination, $\sim 10 \text{ mW cm}^{-2}$, on the cathode shown in Figure 3-8, where the emitted current is larger in the dark than with the light on. In the dark, measurable emission occurs for potentials as low as 150 V across the diamond. With the light on, the emission is reduced and no measurable emission is obtained until a potential in excess of 1 kV is applied. If the cathode is illuminated with no applied potential and then tested in the dark, the emission at the start of the experiment is nearly identical with the emission measured in the light. However, after the emission current exceeds 10^{-7} A , the behavior changes and the characteristics below 2.5 kV are nearly identical with emission in the dark.

This can be explained as follows. When the diamond is illuminated at low applied voltages, the dopants near the diamond surface are photoneutralized, so the electric field at the metal-diamond-vacuum triple junction is not sufficient to cause emission. At larger potentials, $>2.5 \text{ kV}$, significant emission occurs, which can reionize these dopants faster than they can be photoneutralized. In this case sufficient electric field will develop to enhance emission. Once the dopants are neutralized, emission even in the dark will be poor until sufficient potential is applied across the diamond to reionize them.

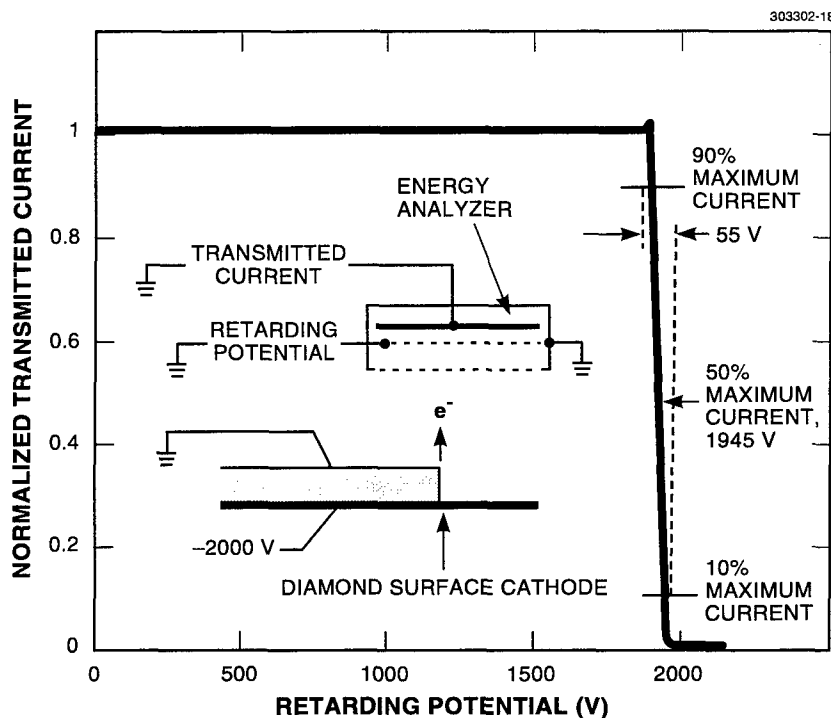


Figure 3-10. Energy analysis of emitted electrons. A retarding energy analyzer can be used to estimate the electron's energy, because the electrons are emitted as a collimated beam from the edge of the diamond. The inset shows a schematic drawing of the experiment.

These results indicate that the triple junction has an important effect on the operation of the this cathode. The initial test devices demonstrated high emission currents and low gate electrode currents. Relatively high operating voltages were required because thick diamond films were used in these devices. Practical cathodes, which would be suitable for flat-panel displays and rf devices, will require the development of a thin-film cathode. This is the subject of the current research.

M. W. Geis	N. N. Efremow
K. E. Krohn	J. C. Twichell
T. M. Lyszczarz	

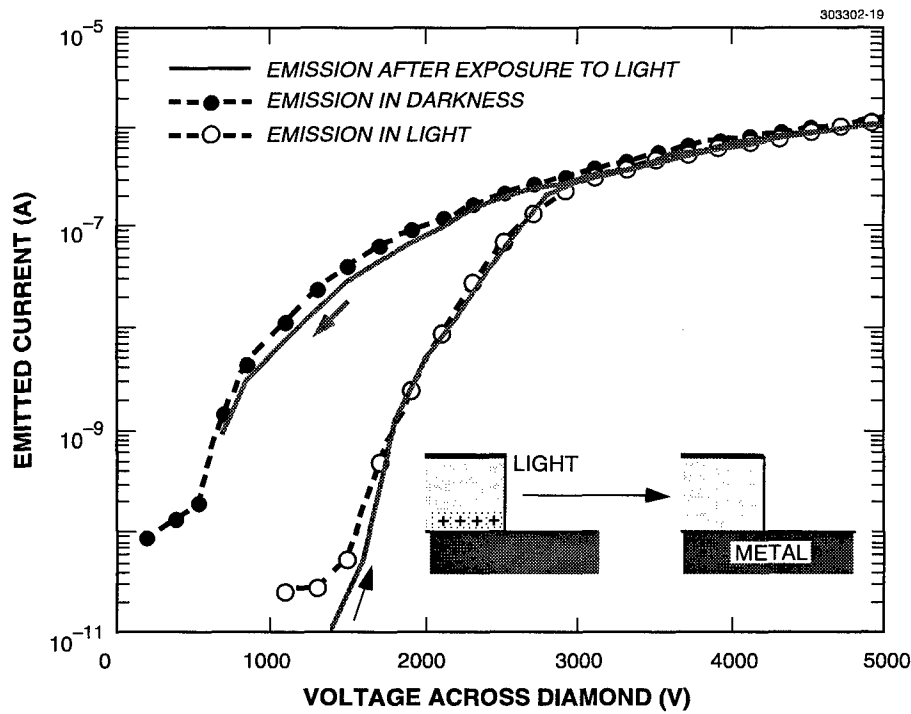


Figure 3-11. Emission current with and without incandescent illumination from a fiber lamp. The filled circles indicate the normal emission characteristics measured in the dark. The open circles show the effects of illumination on emission. The lower curve was obtained in the dark after 1 min of illumination, and it shows the recovery of the emission after the illumination has been removed. The inset shows a possible explanation of the observed reduction in emission with light, where the illumination neutralizes positive charges near the triple junction.

REFERENCES

1. V. N. Ishchenko, S. A. Kochubei, and A. M. Razhev, *Sov. Tech. Phys. Lett.* **12**, 66 (1986).
2. H. H. Li, *J. Phys. Chem. Ref. Data* **9**, 161 (1980).
3. I. H. Malitson, *J. Opt. Soc. Am.* **55**, 1205 (1965).
4. R. N. Shagam, unpublished.
5. D. N. Batchelder and R. O. Simmons, *J. Chem. Phys.* **41**, 2324 (1964).
6. Y. S. Touloukian, R. K. Kirby, R. E. Taylor, and T. Y. R. Lee, *Thermal Expansion, Nonmetallic Solids* (IFI Plenum, New York, 1977).
7. Y. S. Touloukian, R. W. Powell, C. Y. Ho, and P. G. Klemens, *Thermal Conductivity, Nonmetallic Solids* (IFI Plenum, New York, 1970).

8. S. C. Palmateer, R. R. Kunz, A. R. Forte, and M. Rothschild, *Proc. SPIE* **2438**, 455 (1995).
9. H. Okabe, *Photochemistry of Small Molecules* (Wiley, New York, 1978).
10. M. E. Kordesch, private communication.
11. M. W. Geis, J. C. Twichell, and T. M. Lyszczarz, *Linc. Lab. J.* **8**, 161 (1995); M. W. Geis, J. C. Twichell, and T. M. Lyszczarz, *J. Vac. Technol. B* **14**, 2060 (1996).
12. M. W. Geis, N. N. Efremow, K. E. Krohn, J. C. Twichell, and T. M. Lyszczarz, presented at the DARPA High Definition Systems Information Exchange Conference, Arlington, Va., 23–26 March 1997.
13. C. H. De Troureil and K. D. Srivastava, *IEEE Trans. Electr. Insul.* **EI-8**, 17 (1973).
14. R. V. Latham (ed.), *High Voltage Insulation: The Physical Basis* (Academic, New York, 1981), pp. 229–240.
15. S. Prawer, C. Uzan-Spaguy, G. Braunstein, and R. Kalish, *Appl. Phys Lett.* **63**, 2502 (1993).
16. S. Prawer and R. Kalish, *Phys. Rev. B* **51**, 15711 (1995).
17. M. W. Geis, J. C. Twichell, J. Macaulay, and K. Okano, *Appl. Phys. Lett.* **67**, 1328 (1995).
18. T. W. Mercer and P. E. Pehrsson, to be published.
19. M. W. Geis, J. C. Twichell, N. N. Efremow, K. Krohn, and T. M. Lyszczarz, *Appl. Phys. Lett.* **68**, 2294 (1996).

4. HIGH SPEED ELECTRONICS

4.1 PHASE NOISE OF A RESONANT-TUNNELING RELAXATION OSCILLATOR

An electronic oscillator that produces picosecond pulses with excellent timing stability and that can be phase locked to an external clock would be a benefit for certain high-speed signal-processing applications. Two examples are clocks that gate sampling circuits in digital oscilloscopes [1] or that reduce the timing jitter in the front end of high-performance analog-to-digital converters. Presently, optoelectronic conversion can generate pulses with excellent timing stability if a mode-locked laser is used. Also, nonlinear transmission lines that are periodically loaded with varactor or resonant-tunneling diodes (RTDs) [2]–[4] can be driven with a sinusoidal oscillator to generate shock waves. An alternative is the resonant-tunneling relaxation oscillator (RTRo), which can be thought of as a single unit cell of a resonant-tunneling transmission line that is in series connection with a cavity formed by a quarter wavelength of short-circuited transmission line [5]. This report presents measurements of very low phase noise and timing jitter for the pulse train emitted by an RTRo that was injection locked to a sinusoidal waveform.

Figure 4-1(a) shows the equivalent circuit for the RTRo. The key feature is that the RTD is connected in series with a length L_d of transmission line that is terminated by a short circuit. During oscillation, the voltage repeatedly switches between two dc-stable points that are above and below the negative differential resistance (NDR) region in voltage. Since the metastable points are not in the NDR region, the

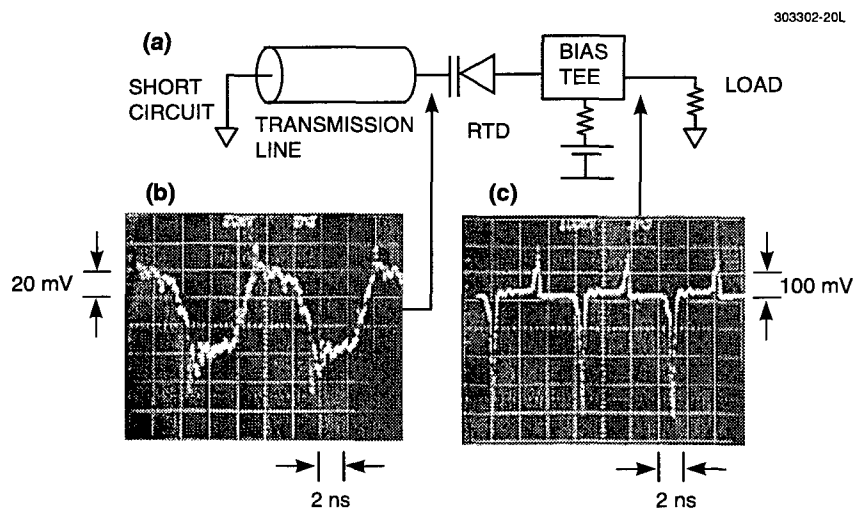


Figure 4-1. (a) Circuit diagram and voltage waveforms measured with a sampling oscilloscope having temporal resolution ~ 25 ps. (b) Square wave output representing the voltage across the resonant-tunneling diode (RTD). (c) Pulsed output voltage measured across the load. The load voltage is proportional to the current passing through the RTD.

RTRO does not require a dc-stable point in the negative resistance region, thereby facilitating the dc biasing of high-current, high-speed diodes. Relaxation oscillations are initiated by manually adjusting the dc bias voltage until the quiescent point is just below the current peak or just above the current valley where a noise fluctuation can start the oscillation. The short-circuited transmission line presents an rf open circuit to the RTD since L_d is an odd multiple of $\lambda/4$ for all harmonics of the oscillator output. The RTD is therefore current biased at rf frequencies, and the two metastable points occur at different voltages but at the same current. The RTRO only emits power to the load during each switching event when a current pulse feeds through the small capacitance of the RTD. This behavior has been verified theoretically with SPICE simulations [5].

Fabrication of the RTD was described previously [5]. In brief, the RTD layers were grown by molecular beam epitaxy on an InP substrate with two 1.7-nm-thick AlAs barriers separated by a 4.8-nm-wide $\text{In}_{0.53}\text{Ga}_{0.47}\text{As}$ quantum well. The area of the mesa-type device was $\sim 40 \mu\text{m}^2$ with peak current density $3 \times 104 \text{ A/cm}^2$, peak-to-valley current ratio 4.9, and peak-to-valley resistance roughly 50Ω . After fabrication, individual devices were whisker contacted inside a quartz-encapsulated cartridge that was mounted in series with the center conductor of a coaxial transmission line. A dc bias was supplied by a battery through a bias tee with 40 GHz of bandwidth. The rf load resistance was 50Ω and was supplied by either a coaxial termination or by the input resistance of the sampling head on an oscilloscope. Figure 4-1(b) shows a measured waveform for the voltage across the relaxation oscillator. Figure 4-1(c) shows a measured waveform for the current through the 50Ω load resistor and hence the RTD. The current waveform resembles the time derivative of the voltage waveform because of the capacitive nature of the RTD.

The conceptual similarity between the RTRO and a mode-locked laser in a linear cavity suggests that this system may have similarly low timing jitter when injection locked [6]. A weak sinusoidal voltage was injected from a synthesizer in series with a 500Ω resistor that was connected to the node between the bias tee and the RTD shown in Figure 4-1(a). The injected signal was 40 dB below the output signal. When the injected signal frequency was tuned near the free-running frequency, the RTRO became synchronized and, at 1.1 GHz, the linewidth narrowed from 1 kHz to <10 Hz—an upper limit imposed by the resolution bandwidth of the spectrum analyzer. Changing the frequency of the injected signal pulled the frequency of the RTRO. The locking range was limited to $\sim 1\%$ of the oscillation frequency and was found to be approximately proportional to $(P_i P_o)^{1/2}$, where P_o is the output power and P_i is the injected power. This behavior is the same as that observed for injection locking of conventional negative-resistance oscillators operating in the small-signal limit [7]. For 3-GHz operation, the synchronization signal was injected through a circulator rather than the 500Ω resistor used at 1.1 GHz. The circulator was used to present a matched load to the output port of the RTRO. In this configuration the maximum locking range was 163 MHz, corresponding to a fractional locking bandwidth of $\Delta f/f = 5\%$.

Subharmonic injection locking at 1.1-GHz repetition frequency was observed down to the 12th subharmonic. The power required for injection locking, however, increased substantially at the lowest subharmonics. Figure 4-2 shows a plot of the injection-locking gain—the ratio of the measured output power to the injected power. An attempt was made to measure each point with approximately the same locking range. The fundamental injection-locking gain of 51 dB is comparable to what can be achieved for

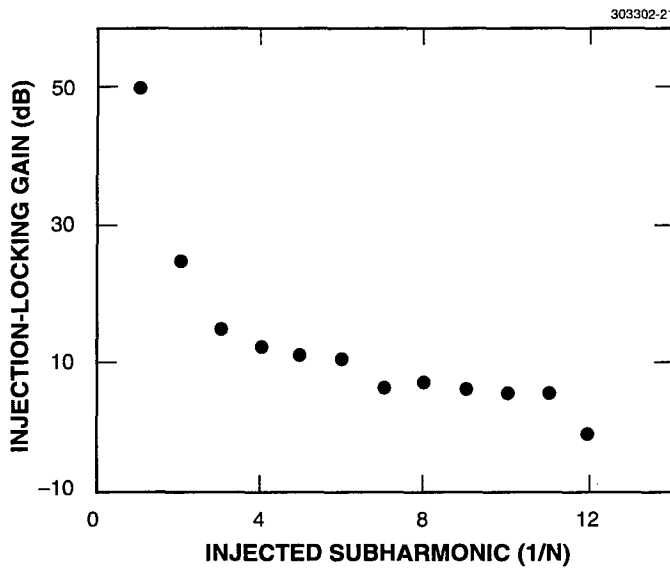


Figure 4-2. Injection-locking gain for fundamental and subharmonic locking.

sinusoidally operating field-effect transistor oscillators with similar locking bandwidth [8]. The injected sinusoidal signal was supplied by a commercial synthesizer [9] that had FM sidebands caused by 60-Hz line noise ~ 50 dB below the carrier. These sidebands were exactly reproduced with 51 dB of amplitude gain at the output of the RTRO, demonstrating the well-known ability of injection-locked oscillators to function as FM amplifiers [7].

Timing jitter between pulses of the injection-locked RTRO was deduced from the phase noise $L_1(f)$ of higher harmonics following the method used by von der Linde for characterizing the timing jitter of mode-locked lasers [6]. The resolution bandwidth of the spectrum analyzer was 10 Hz. This allowed us to set an upper limit on the phase noise contributed by the RTRO by measuring the phase noise away from the carrier at discrete frequency points that were in the valleys between the 60-Hz sideband peaks from the synthesizer.

Table 4-1 shows the phase noise (0.1 and 1 kHz away from the carrier) and timing jitter measured for the RTRO when it was fundamentally injection locked at 1.142 GHz. For comparison, entries are shown that were deduced from measurements at the first, fifth, and tenth harmonics. The timing jitter was estimated by subtracting the 60-Hz sidebands and estimating the spectral area under the sideband curve. The fractional timing jitter $\Delta T/T$, where T is the period, is approximately one to four times better, respectively, than the timing jitter for mode-locked Ti:sapphire and dye lasers that operate with ~ 100 -MHz repetition frequency [10]. Table 4-2 shows the phase noise and timing jitter measured under similar conditions,

TABLE 4-1
Phase Noise and Timing Jitter for Fundamental ($N = 1$)
Injection Locking at 1.142 GHz

f/f_0	f (GHz)	L_1 (100 Hz)	L_1 (1 kHz)	δT [>100 Hz]
1st	1.1	-72 dBc/Hz	-80 dBc/Hz	~200 fs
5th	5.7	-74 dBc/Hz	-81 dBc/Hz	
10th	11.4	-69 dBc/Hz	-80 dBc/Hz	

TABLE 4-2
Phase Noise and Timing Jitter for Fundamental ($N = 1/5$)
Injection Locking at 228 MHz

f/f_0	f (GHz)	L_1 (100 Hz)	L_1 (1 kHz)	δT [>100 Hz]
1st	1.1	-62 dBc/Hz	-73 dBc/Hz	~880 fs
5th	5.7	-62 dBc/Hz	-72 dBc/Hz	
10th	11.4	-60 dBc/Hz	-68 dBc/Hz	

except that the injected signal was 228 MHz—one fifth of the free-running frequency. Compared to fundamental injection locking, the phase noise increased by ~10–12 dB and the timing jitter by ~6 dB. One explanation for the degradation is that phase noise on the injected signal was multiplied up by a factor 25 (14 dB) for 1/5-subharmonic injection locking and exceeded the intrinsic phase noise in the RTRO. If that is the case, the measured phase noise and timing jitter of the subharmonically locked RTRO are an upper limit that could be reduced by injecting a signal with lower phase noise.

Thus, an RTRO has been shown to emit 30-ps-wide voltage pulses at 1.1-GHz repetition frequency with rms timing jitter as low as 200 fs. The RTRO is an electronic source of sharp pulses whose timing jitter compares favorably with mode-locked lasers. Such an oscillator could be used for precision-timing

applications, such as reducing the aperture jitter in the sample-and-hold stage of high-speed analog-to-digital converters.

S. Verghese
C. D. Parker
E. R. Brown

REFERENCES

1. L. Yang, S. D. Draving, D. E. Mars, M. R. T. Tan, *IEEE J. Solid-State Circuits* **29**, 585 (1994).
2. D. W. van der Weide, J. S. Bostak, B. A. Auld, and D. M. Bloom, *Appl. Phys. Lett.* **62**, 22 (1993).
3. C. L. Dennis, E. R. Brown, and S. Prasad, *Proceedings of the International Semiconductor Device Symposium* (University of Virginia, Charlottesville, Va., 1993), p. 465.
4. R. Y. Yu, Y. Konoshi, S. T. Allen, M. Reddy, and M. J. Rodwell, *IEEE Microwave Guided Wave Lett.* **4**, 220 (1994).
5. E. R. Brown, C. D. Parker, S. Verghese, and J. F. Harvey, *Appl. Phys. Lett.* **70**, 2787 (1997).
6. D. von der Linde, *Appl. Phys. B* **39**, 201 (1986).
7. K. Kurokawa, *Proc. IEEE* **61**, 1386 (1973).
8. X. Zhang, X. Zhou, and A. S. Daryoush, *IEEE Trans. Microwave Theory Tech.* **40**, 895 (1992).
9. HP synthesized sweeper, model 8340A.
10. J. Son, J. V. Rudd, and J. F. Whitaker, *Opt. Lett.* **17**, 733 (1992).

5. MICROELECTRONICS

5.1 GEIGER-MODE AVALANCHE PHOTODIODE ARRAYS FOR IMAGING LASER RADAR

The performance of an imaging laser radar depends on its time measurement resolution and on a combination of its detection sensitivity and transmitter power. An avalanche photodiode (APD) operated in the Geiger mode (biased above breakdown) can give a fast, large-amplitude signal in response to a single photon. Monolithic APD arrays can be incorporated into lightweight receiver electronics. The gain provided by such sensitive detectors in airborne laser radar systems can enable substantial reductions in the payload weight and volume required for transmitter components such as laser amplifiers.

We have fabricated monolithic arrays of silicon APDs for operation at 532 nm, and are developing wafer-to-wafer bonding approaches to integrate these arrays with high-speed CMOS timing circuits. The APD is a $p^+ - p - p - p - n^+$ structure formed by epitaxial growth of a lightly boron doped (10^{14} cm^{-3}) silicon layer on a p^+ silicon substrate, followed by ion implantation of boron and arsenic to form the upper p region and the n^+ contact layer, respectively. The lower p layer is for absorption of incident photons, and the upper p layer, which is roughly 0.5 mm thick, is the avalanche region, where photoelectrons initiate impact ionization. Details of the device structure and fabrication process were reported previously [1].

When operated in the Geiger mode, the APD is charged to some initial bias above the breakdown voltage. When an avalanche occurs, due either to the absorption of a photon or to dark current, the APD discharges down to slightly below the breakdown voltage. By measuring the average frequency of these pulses both in the dark and in the presence of a calibrated incident photon flux at 532-nm wavelength, the external quantum efficiency of the device can be inferred. We have measured quantum efficiencies approaching 40% on the best front-illuminated uncoated devices fabricated on 6-in.-diam silicon wafers. Based on this data, the projected quantum efficiency for an antireflection-coated back-illuminated device is close to 100%.

When used in a three-dimensional laser radar receiver, Geiger-mode APDs are used to measure the time of arrival of photons scattered from a target illuminated by a short laser pulse. In order to measure this time accurately the APD must have low timing jitter. This was measured by illumination of a fixed-range target by 250-ps pulses from a doubled Nd:YAG microchip laser. The pulse energy was attenuated so that the detection probability was low (10%), and a histogram of photon return times measured by one of the APDs was built up. This is shown in Figure 5-1, and has a width of 291 ps, to which the duration of the laser pulse is the major contributor. If this pulse is assumed to be Gaussian, the intrinsic timing jitter of the APD and measuring electronics is inferred to be 140 ps.

Avalanches initiated by dark current raise an important issue since such “dark counts” set a lower limit on the false-alarm rate. The APDs that have good quantum efficiency have dark-count rates in the 20–40-kHz range at room temperature. The responsible dark current is believed to come from bulk thermal generation, so substantial reduction of dark-count rates can be achieved with modest cooling of the devices.

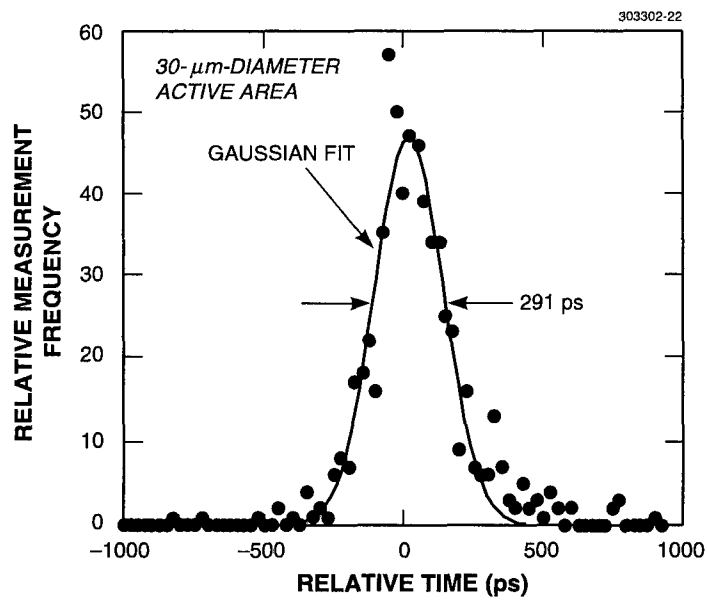


Figure 5-1. Distribution of photon return times from fixed-range target as measured by an avalanche photodiode.

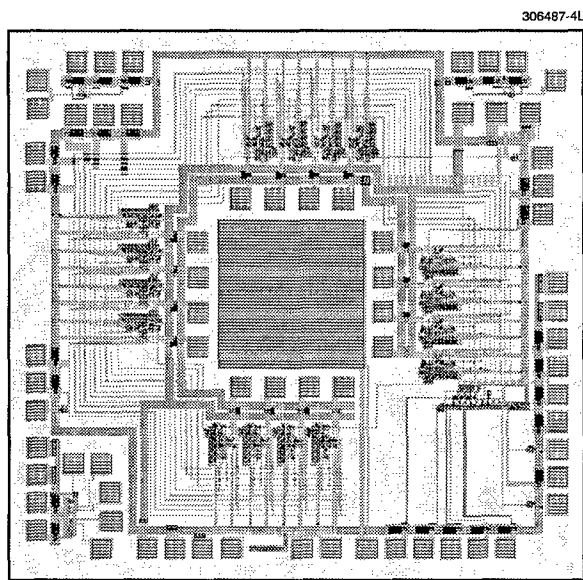


Figure 5-2. Mask layout for the MOSIS CMOS timing chip.

Figure 5-2 shows the chip layout of a mask layout of a MOSIS 0.5- μ m CMOS chip that will provide clock generation and timing circuitry for a 4×4 APD array. The APD array will be attached to the large pad in the center of the chip and the individual diodes wire bonded to the internal bonding pads. The circuit, which is currently being fabricated, is expected to provide 19 bits of timing information for each pixel, with the least significant bit representing a 0.5-ns interval.

B. F. Aull

REFERENCE

1. Solid State Research Report, Lincoln Laboratory, MIT, 1996:3, p. 39.

6. ANALOG DEVICE TECHNOLOGY

6.1 TUNABLE SUPERCONDUCTING RESONATORS USING FERRITE SUBSTRATES

Planar tunable microwave resonators that combine superconducting microstrip circuits with ferrite substrates have been demonstrated, and exhibit performance exceeding that of conventional technology. These resonators are a key element of tunable multipole bandpass filters now under development. The goal is to provide wideband tunability with the previously demonstrated [1] advantages of low loss, sharp skirts, and compact size of planar filters based on high-temperature superconductivity (HTS).

The tunable superconducting resonators that have been demonstrated use microstrip circuits of YBCO at 77 K and niobium at 4 K coupled to polycrystalline magnetic garnet substrates. Polycrystalline ferrite was chosen because the material is readily available in sizes needed for multipole filters, is inexpensive, and supports high- Q operation. In addition, the polycrystalline materials may readily be altered in chemical composition to optimize properties such as saturation magnetization and coercive field for cryogenic operation. For both devices we employed a planar microstrip geometry with an $n/2$ resonator whose characteristic impedance is $\sim 50 \Omega$ (width is $230 \mu\text{m}$ and substrate thickness is $380 \mu\text{m}$ for the niobium-on-ferrite devices). An external magnetic field was applied in the plane of the substrate and parallel to the propagation direction of the microstrip.

The YBCO resonator is configured with a YBCO microstrip on LaAlO_3 that is clamped to the polycrystalline ferrite substrate. Placing the ferrite in intimate contact with the YBCO stripline allows the strong interaction of the rf magnetic fields of the superconductor with the magnetization of the ferrite [2] and thus provides a tuning mechanism.

Figure 6-1 shows results of measurements of the Q and resonance frequency f_0 of one of the YBCO resonators as a function of the applied magnetic field at 77 K. This device showed a Q of ~ 2500 and a tunability of 3% for applied fields of ~ 100 Oe. Most of the tuning takes place at very low fields, indicating that the magnetization of the substrate is responsible for the effect. The figure of merit $2Q\Delta f/f$ for this resonator is 172. We have measured separately the Q of the YBCO resonator at 77 K. At 7.7 GHz the Q was 5800 without ferrite. Thus, we conclude that either the ferrite losses or the parasitic losses of the clamped structure are limiting the Q of the YBCO tunable resonators.

The second device reported here is fabricated from superconducting niobium deposited directly on a ferrite substrate, which also includes a ground plane. Figure 6-2 shows the Q and f_0 for a niobium resonator on ferrite. This device showed a Q of 5000 and a tunability of 3%. The figure of merit is 288. Figure 6-3 shows the resonance frequency vs applied magnetic field from a longer sample with lower frequency than that of Figure 6-2 and measured with finer resolution. The tunability range in this case is 6% for fields below 100 Oe. This device also shows hysteresis around zero field, indicating that the magnetization of the substrate is having an important influence on the resonance frequency. Most of the tuning occurs at low field, just above the coercive field of the ferrite where the magnetization is changing rapidly with the magnetic field.

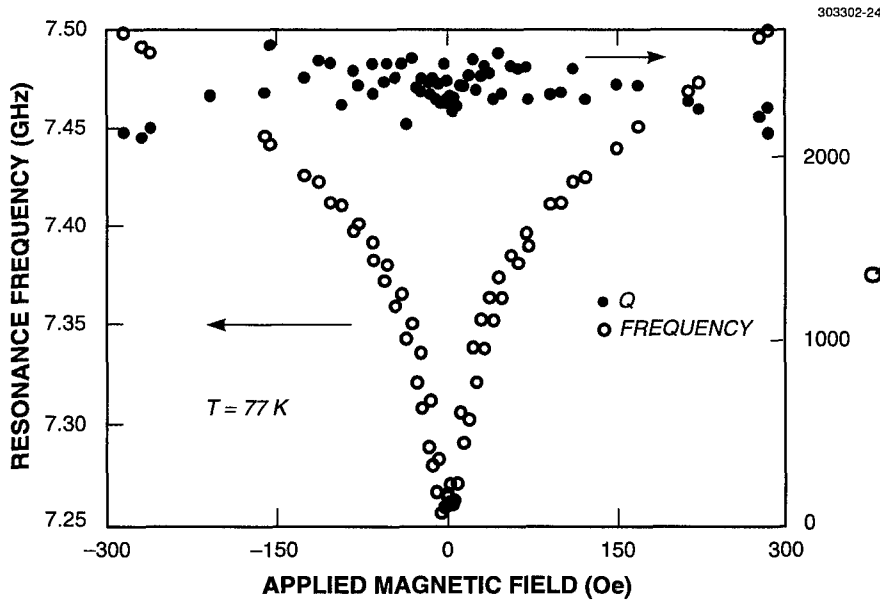


Figure 6-1. Plot of f_0 (open circles, left scale) and Q (closed circles, right scale) vs applied field for a YBCO microstrip resonator on a LaAlO_3 substrate coupled to polycrystalline iron garnet.

A new analytical model has been developed [3] that treats the partially magnetized state of the ferrite, and takes into consideration the hysteresis loop and the demagnetizing effects of the microstrip geometry. The effective permeability of the microstrip on the ferrite configuration is determined to be

$$\mu_{\text{eff}} = 1 + \left\{ \frac{(\gamma 4\pi M)\gamma [H + (N_y - N_z)4\pi M]}{f_r^2 - f^2} \right\}, \quad (6.1)$$

where f is the signal frequency, f_r is the ferrimagnetic resonance frequency, γ is the gyromagnetic factor = 2.8 MHz/Oe, H is the applied magnetic field, $4\pi M$ is the magnetization of the ferrite, N_z is the geometric demagnetizing factor in plane along the direction of propagation, and N_y is the effective demagnetizing factor of the rf magnetization component normal to the plane. In these experiments the $f_r \ll f$ and H are small compared with $4\pi M$. For the stripline geometry we can approximate $N_y \approx 0.37$ and $N_z \approx 0.02$ so the final result to be compared with the experiments is

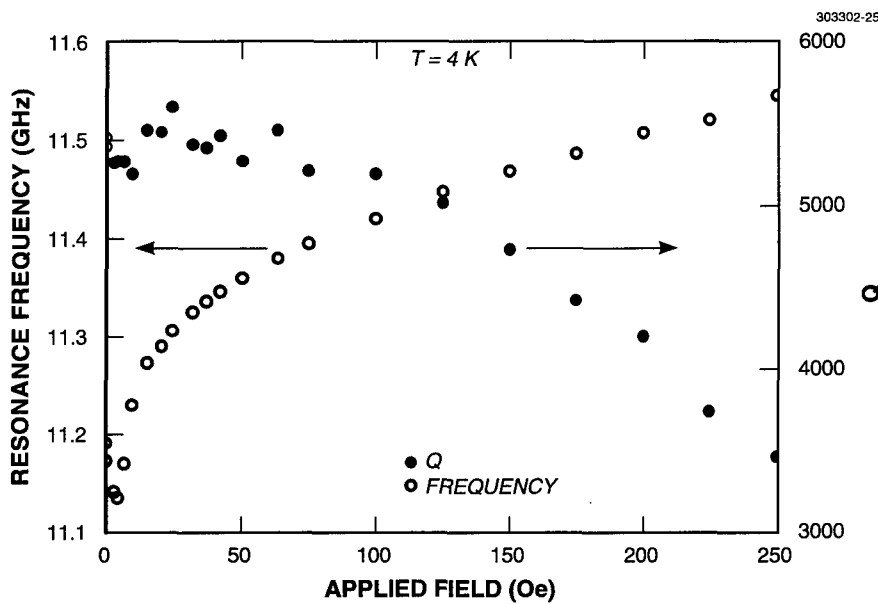


Figure 6-2. Plot of f_0 (open circles, left scale) and Q (closed circles, right scale) vs applied field for a niobium microstrip resonator on a polycrystalline iron garnet substrate.

$$\frac{f(H)}{f(0)} = 1 + \frac{1}{2} \frac{\gamma 4\pi M \gamma (H + (N_y - N_z) 4\pi M)}{f^2}, \quad (6.2)$$

where $M = M(H)$ is a function of H governed by the hysteresis loop of the ferrite. This is the expression that is plotted as the solid line in Figure 6-3 and compared with experiment. As can be seen the agreement is excellent.

Since most of the tunability that we observe results from changes in the magnetization, a practical tuning circuit need only supply magnetic fields of the order of the coercive fields of the ferrites which are usually less than about 10 Oe. Such fields can be achieved with simple magnetic structures and therefore can be made consistent with short time constants needed for fast tunability on the order of 1 μ s or less. It is also possible to provide the necessary tunability by the remanent magnetization of the ferrite in a closed magnetic circuit, thus eliminating the need to maintain a steady-state magnetic field and requiring only pulsed operation of the applied field to change the magnetization of the substrate. Well-known flux-drive techniques [4] can be used to provide continuous accurate tuning over the tunable frequency range.

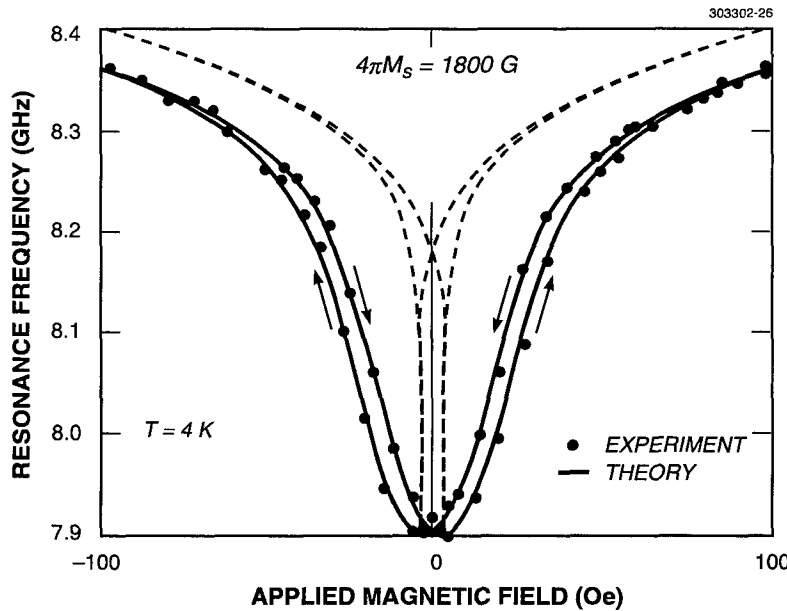


Figure 6-3. Plot of f_0 vs applied field for a niobium microstrip resonator on a polycrystalline iron garnet substrate. Points are measured data and the solid line is the model discussed in the text, with $N_z = 0.02$. The dashed line is for $N_z = 0$.

Thus, we have demonstrated resonators with wide tunability and high Q by using superconductors on ferrite substrates. The tunability occurs at low magnetic fields so that a very simple coil can provide the necessary field, and time constants can be kept low so that rapid tuning is possible. This demonstration provides great promise for tunable multipole filters in compact form at microwave frequencies.

D. E. Oates
G. F. Dionne

REFERENCES

1. Solid State Research Report, Lincoln Laboratory, MIT, 1996:2, p. 29.
2. G. F. Dionne, D. E. Oates, D. H. Temme, and J. A. Weiss, *IEEE Trans. Microwave Theory Tech.* **44**, 1361 (1996).
3. G. F. Dionne and D. E. Oates, *IEEE Trans. Magn.* **33**, 3421 (1997).
4. W. J. Ince and D. H. Temme, *Adv. Microwaves* **4**, 1 (1969).

7. ADVANCED SILICON TECHNOLOGY

7.1 FULLY DEPLETED SILICON-ON-INSULATOR TECHNOLOGY DEVELOPMENT

A sub-0.25- μm fully depleted silicon-on-insulator (FDSOI) technology which is targeted for sub-1-V circuit operation has been developed at Lincoln Laboratory [1]. The fully depleted design results in an enhanced subthreshold slope (65–75 mV/decade) allowing transistor thresholds in the $\pm 400\text{-mV}$ range. Compared to a conventional 0.5- μm CMOS technology, the low-power SOI technology represents a 36-fold reduction in power consumption for comparable circuit performance and a twofold performance enhancement with a tenfold power reduction when operated at the design voltage of 1 V. In addition, the absence of body contacts permits a more compact circuit layout. The initial experiments utilized one level of metal, but the back end processing has been extended to a fully planar three-level metal process which incorporates damascene hot aluminum plugs at contacts, via 1 and via 2, and planarization of two plasma-deposited intermetal oxides by chemical-mechanical polishing [2]. This has been further improved by implementation of a cobalt silicide technology to reduce source-drain extrinsic resistance [3].

FDSOI has been proposed for low-power applications such as remote land- and space-based sensors which must operate unattended for extended periods. FDSOI combined with deep-submicrometer optical lithography has also been proposed to satisfy the high-bandwidth requirements of wireless communication systems which must operate with minimal power consumption. Because of the unique properties of FDSOI, collaboration between integrated circuit design and technology development is necessary if the potential of the technology is to be realized. To further that collaboration, HSPICE parameters were extracted from test transistors, and design rules were written in order that researchers in the low-power community could design and characterize circuits fabricated with the FDSOI technology. The principal rules are listed in Table 7-1 and the photolithography levels in Table 7-2. Sixteen organizations including Lincoln Laboratory submitted 29 designs which were incorporated into a multiproject SOI chip. Upon completion of wafer fabrication, the individual circuits were cut from the SOI chips and sent to the designers for characterization.

Device results were reported by the following companies and institutions: (1) At Boeing a 2-K static random-access memory was operated at the limit of the tester (300 MHz) at 2 V. The circuit functioned down to a 0.6-V power supply. (2) At Rockwell (Boeing) a 12-bit analog-to-digital (A/D) converter was designed to operate at 0.8 M-samples/second and 80 μW . The key elements of the circuit were functional. (3) At Lucent, functional digital signal processing circuits for wireless communications systems were obtained. (4) At Irvine Sensors, low-noise mixed-mode analog and neural circuits were functional. Test board limitations prevented characterization of the circuits' speed. (5) At Arizona State, functional current mode A/D converters were obtained. (6) At MIT, functional digital test circuits were obtained with 11 000 transistors.

TABLE 7-1
Fully Depleted Silicon-on-Insulator Process and Design Parameters

Parameter	Value
Initial silicon-on-insulator (SOI) thickness	62 nm
Buried oxide (BOX) thickness	200 nm
Sidewall oxide thickness	25 nm
Gate oxide thickness	8 nm
Spacer thickness	120 nm
Deposited oxide thickness	450 nm
<i>n</i> -channel body doping	$4.0 \times 10^{17}/\text{cm}^3$
<i>p</i> -channel body doping	$3.5 \times 10^{17}/\text{cm}^3$
<i>n</i> -channel moderately doped drain (MDD) doping	$8 \times 10^{19}/\text{cm}^3$
<i>p</i> -channel MDD doping	$4 \times 10^{19}/\text{cm}^3$
<i>n</i> ⁺ , <i>p</i> ⁺ -poly sheet rho	14 Ω/sq (silicided)
<i>n</i> ⁺ , <i>p</i> ⁺ sheet rho	14 Ω/sq (silicided)
Metal-1 sheet rho	0.06 Ω/sq
Minimum island width	0.5 μm
Minimum island spacing	0.6 μm
Minimum gate length	0.25 μm
Minimum gate spacing	0.35 μm
Minimum metal-1, -2 width	0.75 μm
Minimum metal-1, -2 spacing	0.75 μm
Minimum metal-3 width	1 μm
Minimum metal-3 spacing	1 μm
Contacts	$0.5 \times 0.5 \mu\text{m}^2$
Vias	$0.75 \times 0.75 \mu\text{m}^2$

An internally designed chip which included approximately 5000 transistors was included in the multiproject SOI chip. The circuit was designed to perform a high-speed comparison on two 8-bit words and, based on the results, either store or discard the information. The application requires an 800-MHz clock rate at a 2-V power supply; the chip was fully functional at 1 GHz and 2 V [4].

A second multiproject chip was assembled from 25 designs submitted from 19 external organizations and six Lincoln Laboratory groups, using design rules which were modified based upon test results from the initial chip. The second multiproject chip is being fabricated.

The effect of ionizing radiation on the characteristics of FDSOI *n*-channel transistors was investigated to determine the applicability of the technology to space applications. Since the off-state leakage and threshold of a FDSOI transistor are functions of the gate, sidewall, and buried oxide properties, radiation-induced changes in any of those oxides will modify the transistor's properties. An ARACOR 4100 10-keV x-ray source was used to irradiate transistors with 0.5- μm gates and 200-nm buried oxides in increments from 10 to 80 krads. The gates were biased at 1 V and the substrates, sources, and drains grounded during irradiation. Transistors with 8- and 25-nm sidewall oxides were investigated. The front and back channel thresholds decreased approximately 0.08 and 1.7 V, respectively, after 80 krads due to an increase of charge in the gate and buried oxides. More noteworthy are the results shown in Figure 7-1 where the device with 8-nm sidewall oxide developed considerably less sidewall leakage than the device with a 25-nm oxide. The effect of charge buildup on the flat band of a MOS capacitor due to ionizing radiation is proportional to the square of the oxide thickness. Thus, the threshold of the edge transistor with the 8-nm sidewall oxide was far more resistant to ionizing radiation. This result indicates that an 8-nm sidewall oxide permits the FDSOI technology to satisfy low-level radiation exposure requirements without requiring process changes to harden oxides.

Threshold control in a FDSOI technology is complicated by the dependence of threshold on silicon thickness, so experiments were conducted to determine if threshold control would be dominated by thickness variations in the starting silicon material. The thresholds of 100 *n*-channel transistors with 0.5- μm gates were analyzed in terms of silicon thickness, sidewall implant dose, channel implant dose, channel implant energy, and drift region dose. The data were obtained from seven SIMOX wafers with 380-nm buried oxides; the silicon thickness at each test site was obtained from wafer mapping measurements after the thinning oxidation. A five-factor interaction model was constructed using response surface analysis techniques and the results used to determine the effects of a 10% process variation on threshold; the correlation between the data and the model was 0.93. The results listed in Table 7-3 show that variations in channel implant dose had the greatest effect on threshold, but silicon thickness and channel implant energy are nearly as important and also indicate that the implant energy must be tuned to the starting silicon thickness.

Obtaining low-resistance contacts to thin silicon layers is a major challenge for FDSOI technology. A 49-stage ring oscillator with 0.25- μm gate lengths was used to correlate the effects of extrinsic transistor resistance with inverter delay; the resistance was determined [5] from transistors whose gate lengths ranged from 0.2 to 0.5 μm . The study involved 60 ring oscillators from eleven SIMOX wafers with

TABLE 7-2
Fully Depleted Silicon-on-Insulator Photolithography Levels

Layer	Function
Active	Define SOI island
<i>p</i> -channel	Implant <i>n</i> -channel sidewalls
<i>n</i> -channel	Implant <i>p</i> -channel sidewalls
<i>p</i> -channel	Implant <i>n</i> -channel body
<i>n</i> -channel	Implant <i>p</i> -channel body
Poly	Define gates and interconnect
<i>n</i> ⁺ implant	Implant <i>n</i> MDD regions
<i>p</i> ⁺ implant	Implant <i>p</i> MDD regions
<i>n</i> ⁺ implant	Implant <i>n</i> ⁺ regions
<i>p</i> ⁺ implant	Implant <i>p</i> ⁺ regions
Contact	Define active and poly cuts
Metal 1	Define metal-1 interconnect
Via 1	Define metal-1/metal-2 vias
Metal 2	Define metal-2 interconnect
Via 2	Define metal-2/metal-3 vias
Metal 3	Define metal-3 interconnect
Pads	Define overglass cuts

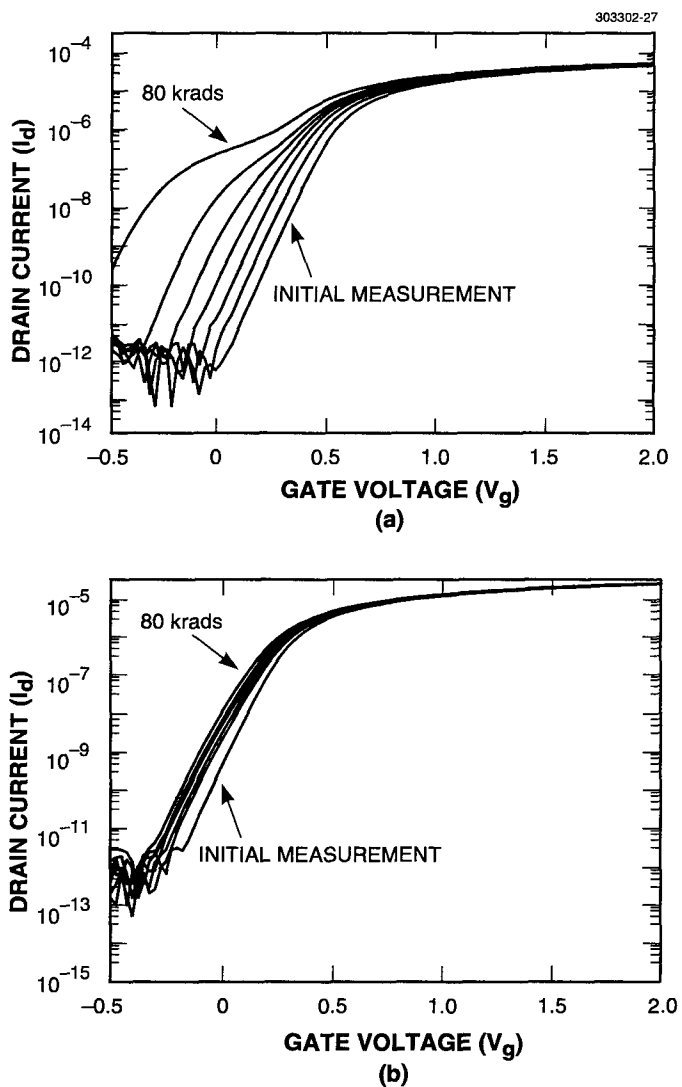


Figure 7-1. I_d plots of an n-channel fully depleted silicon-on-insulator (FDSOI) device with (a) 0.25-nm sidewall oxide and (b) 8-nm sidewall oxide. Shown are the initial and postradiation characteristics at 10, 20, 30, 40, 50, and 80 krads. Gate length and width are 0.25 and 7 μm , respectively; drain voltage is 0.05 V.

TABLE 7-3
Effects of 10% Process Variations on 0.25- μm Parameters

Process Factor	Nominal Value	Threshold Variation (mV)
SOI thickness	60 nm	25
Sidewall implant dose	$2.5 \times 10^{13}/\text{cm}^2$	0.2
Channel implant dose	$3.5 \times 10^{12}/\text{cm}^2$	32
Channel implant energy	25 keV	18
MDD dose	$5 \times 10^{14}/\text{cm}^2$	-10

200-nm buried oxides in which variations in silicide processing were investigated. The results summarized in Figure 7-2 show the stage delay at 2 V as a function of *n*- and *p*-channel extrinsic resistance and indicate that the *p*-channel contacts were the principal cause of excessive delay; threshold variations account for the scatter at resistances less than 1000 Ω . Subsequent analysis showed that boron depletion at the silicide-silicon interface resulted in high contact resistance between the silicide and the p^+ silicon. An HSPICE simulation of inverter delay as a function of extrinsic resistance used HSPICE parameters extracted from FDSOI transistors but varied the *n*- and *p*-channel resistances R_{dsw} . The simulation results shown in Figure 7-3 indicate that inverter performance is not degraded substantially for extrinsic resistances less than 360 and 1000 $\Omega \mu\text{m}$ for the *n*- and *p*-channel devices, respectively. These values are achievable with present silicide processing technology.

Transistors and ring oscillators with effective channel lengths $<0.2 \mu\text{m}$ have been fabricated using the technology discussed above. As part of that effort, simulations have been used to define a process which is compatible with a 0.15- μm technology. The standard practice of scaling the channel doping as an inverse function of channel length is constrained by the FDSOI requirement that the maximum depletion depth be greater than the silicon thickness. However, the silicon and buried oxide thicknesses provide two additional degrees of freedom to scale the technology to 0.15 μm [6]. Optimization of those thicknesses is required to produce desired device parameters as well as to minimize the effects of processing variations on those parameters. The simulation and analysis techniques previously reported [7] were used to define a 0.15- μm process which would yield an *n*-channel transistor with off-state leakage at $V_d = 1 \text{ V}$ of 100 pA per μm of channel width, a threshold of 0.4 V, and an inverse subthreshold slope of 73 mV/decade. These

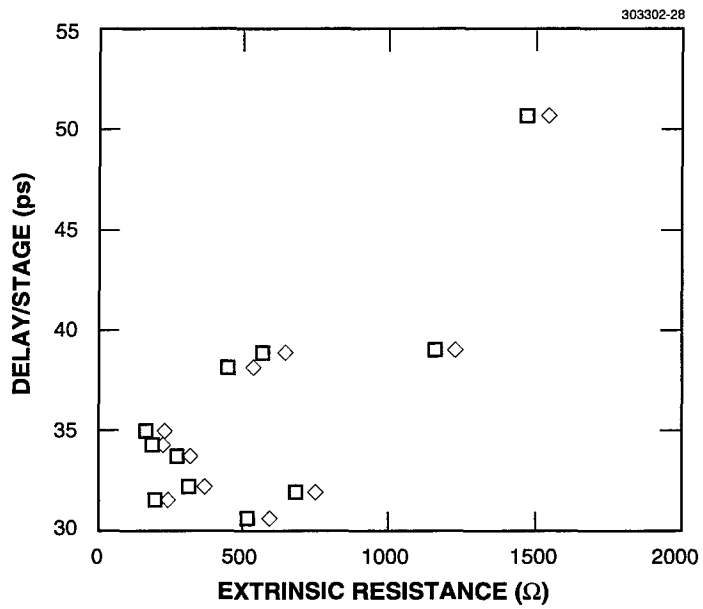


Figure 7-2. Ring oscillator stage delay vs extrinsic resistance extracted from test transistors adjacent to the ring oscillator. The sum of the p- and n-channel resistance (diamonds) and the p-channel resistance (squares) indicates that p-channel resistance variations accounted for the majority of delay.

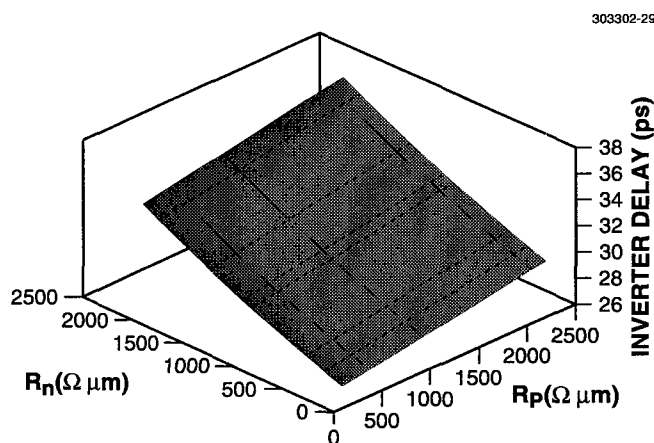


Figure 7-3. Response surface of a 0.25- μm ring oscillator stage delay vs transistor-extrinsic resistance. HSPICE was used to simulate delay using SPICE parameters extracted from FDSOI transistors with the exception of the n- and p-channel resistances which were varied in the simulation.

TABLE 7-4
Effects of 10% Process Variations on 0.15- μm Parameters

Process Parameter	Off-State Leakage	Threshold (mV)
BOX thickness	14	-1.3
SOI thickness	-36	20
Channel implant dose	-104	40
Gate length	-42	10
Total sensitivity	118	46

requirements were met with a 75-nm buried oxide, a starting silicon thickness of 45 nm, a channel implant dose of $6.5 \times 10^{12} / \text{cm}^2$, and 5-nm gate oxide. A moderately doped drain and a boron halo implanted adjacent to the gate were required to reduce the dependence of threshold on gate length. The variations in off-state leakage and threshold due to a 10% increase in buried oxide and silicon thicknesses, channel implant dose, and gate length were simulated. The results listed in Table 7-4 show that drain-source leakage is the parameter most sensitive to process variations. It is dominated by the channel implant dose and is equally affected by silicon thickness and gate length variations. The total variations listed in the table are the root sum of each variation squared and are a measure of the stability of the process. If the buried oxide thickness is increased to 125 nm, the total sensitivity of leakage and threshold increases to 165 pA and 75 mV, respectively. Thus, a thin buried oxide is essential to reduce the sensitivity of device parameters to variations in buried oxide and silicon thickness, channel length, and channel implant dose. These results will be applied to the fabrication of ring oscillators and rf amplifiers with 0.1–0.15- μm gates.

J. A. Burns	C. L. Keast
J. M. Knecht	H. L. Liu
A. M. Soares	P. W. Wyatt

REFERENCES

1. Solid State Research Report, Lincoln Laboratory, MIT, 1996:2. p. 35.
2. J. Knecht, E. Gleason, C. Keast, and J. Reinhold, presented at VLSI/ULSI Multilevel Interconnection Conference, Santa Clara, Calif., 10–12 June 1997.
3. Solid State Research Report, Lincoln Laboratory, MIT, 1996:3. p. 49.
4. Solid State Research Report, Lincoln Laboratory, MIT, 1996:4. p. 41.
5. F. H. De La Moneda, H. N. Kotecha, and M. Shatzkes, *IEEE Electron Device Lett.* **EDL-3**, 10 (1982).
6. M. J. Sherony, L. T. Su, J. E. Chung, and D. A. Antoniadis, *IEEE Electron Device Lett.* **16**, 100 (1995).
7. J. A. Burns and G. R. Young, presented at the Semiconductor Research Corporation Computer-Integrated Manufacturing IC Workshop, Pittsburgh, Pa, 26 August 1993.

REPORT DOCUMENTATION PAGE

Form Approved
OMB No. 0704-0188

Public reporting burden for this collection of information is estimated to average 1 hour per response, including the time for reviewing instructions, searching existing data sources, gathering and maintaining the data needed, and completing and reviewing the collection of information. Send comments regarding this burden estimate or any other aspect of this collection of information, including suggestions for reducing this burden, to Washington Headquarters Services, Directorate for Information Operations and Reports, 1215 Jefferson Davis Highway, Suite 1204, Arlington, VA 22202-4302, and to the Office of Management and Budget, Paperwork Reduction Project 0702-0188, Washington, DC 20503.